The Astrophysical Journal, 940:48 (23pp), 2022 November 20 https://doi.org/10.3847/1538-4357/ac94d2

A Study of the Spectral Properties of Two Gamma-Ray Bursts with the Main Bursts and Postbursts

Tan-Tan Du[1], Zhao-Yang Peng[1], Jia-Ming Chen[1], Ting Li[2], and Yue Yin[3]
[1] College of Physics and Electronics information, Yunnan Normal University, Kunming 650500, People's Republic of China; pengzhaoyang412@163.com
[2] State owned assets and Laboratory Management Office, Yunnan Normal University, Kunming 650500, People's Republic of China
[3] Department of Physics, Liupanshui Normal College, Liupanshui 553004, People's Republic of China
Received 2022 May 29; revised 2022 August 25; accepted 2022 September 23; published 2022 November 18

Abstract

The jet composition in gamma-ray bursts (GRBs) is still an unsolved issue. We try to provide some clues to the issue by analyzing the spectral properties of GRB 160509A and GRB 130427A with a main burst and a postburst. We first perform Bayesian time-resolved spectral analysis and compare the spectral components and spectral properties of the main bursts and postbursts of the two bursts and find that both bursts have the thermal components, and the thermal components are mainly found in the main bursts, while the postbursts are mainly dominated by the nonthermal components. We also find that the low-energy spectral indices of some time bins in the main bursts of these two GRBs exceed the so-called synchronous dead line, and in the postburst, only GRB 160509A has four time bins exceeding the dead line, while none of GRB 130427A exceed the dead line. We then constrain the outflow properties of both bursts and find that the main bursts is consistent with the typical properties of photosphere radiation. Therefore, our results support the transition of the GRB jet component from the fireball to the Poynting-flux-dominated jet. Finally, after analyzing the correlation and parameter evolution of the spectral parameters of the two bursts, we find that the correlations of the spectral parameters have different behaviors in the main bursts and postbursts. The parameter evolution trends of the main bursts and postbursts also show consistent and inconsistent behavior; therefore, we currently cannot determine whether the main bursts and postbursts come from the same origin.

Unified Astronomy Thesaurus concepts: Gamma-ray bursts (629)

1. Introduction

A gamma-ray burst (GRB) is a phenomenon where the gamma rays in cosmic space suddenly intensify and then quickly weaken over a short period. It is the most violent electromagnetic waves observed at the stellar level. Nearly 50 yr after the discovery of GRBs, the transient emission remains puzzling from several basic perspectives, one of which is the very basic question of jet composition (Ruffini et al. 1999; Popham et al. 1999; Ruffini et al. 2000; Di Matteo et al. 2002; Gu et al. 2006; Liu et al. 2007; Zhang & Yan 2011; Zhang 2011; Xue et al. 2013; Bégué & Pe'er 2015; Kumar & Zhang 2015; Liu et al. 2017). We can obtain information on the energy, radiation mechanism, and jet structure of a GRB by studying its spectra. Observations suggest that the GRB spectra may be composed of a thermal and a nonthermal component, with the thermal radiation coming from the fireball photosphere, which can be predicted with the fireball model, and the nonthermal radiation coming from the shocks or magnetic reconnection and turbulence (Rees et al. 1994; Katz 1994; Sari et al. 1996; Daigne & Mochkovitch 1998; Lloyd & Petrosian 2000; Kumar & McMahon 2008; Daigne et al. 2011; Zhang & Yan 2011; Beniamini & Piran 2013, 2014). The popular models used to fit GRB spectra are the simple power law (PL), the cutoff power law (CPL), the band function (Band), and the Planck function.

Previous studies showed that subbursts also known as precursors exist during bursts, and different researchers have given different definitions and explanations for precursors, among which, according to Troja et al. (2010), one is that a precursor should satisfy the following two criteria: (1) the peak flux of the precursor is less than that of the main burst; (2) there are quiescent times between the precursor and the main burst.

Zhang et al. (2018) reported a particularly bright outburst event of GRB 160625B, which has three isolated episodes (a short precursor, a very bright main burst, and an extended radiation event similar to a postburst) separated by two long quiescent intervals (180 and 300 s), and the temporal and time-resolved spectral analysis of the precursor and main burst revealed that the precursor exhibited a thermal spectral component, while the main burst and extended radiation events has a nonthermal component. By further analyzing GRB 160625B, Li (2019) obtained very different spectral properties for the main burst and the precursor, suggesting a possible different origin between the main burst and the precursor. These studies of GRB 160625B reveal a transformation of the jet composition from fireball-dominated to Poynting-flux-dominated. Zhong et al. (2019) selected a sample of short bursts with precursors; they extracted a sample of 18 short bursts with precursors from the 660 short bursts observed by Fermi and Swift and performed temporal and spectral analysis; they found that precursors and main bursts still exhibit some differences, with most main bursts lasting longer than precursors; the average flux of precursors increases as the main burst brightens; most of the precursors and main bursts exhibit nonthermal emission properties; and the precursor may serve as an important probe of the properties of the predecessor stars of the short burst. Coppin et al. (2020) studied short burst data observed by Swift/BAT, focusing on events with both precursors, main bursts, and extended radiation in short bursts. The similarity between main bursts with one main peak and two main peaks was investigated in terms of temporal

structure, and no anomalies were found, with Swift and BATSE observations yielding similar main burst properties for short bursts; the duration of the main burst was also found to be a little longer than the precursor but a little shorter than the extended radiation component; in particular, a correlation was found between the peak fluxes of the precursors, main bursts, and extended radiation, thus supporting the idea that the three events were derived from similar central engine activity. Charisi et al. (2015) collected and analyzed 2710 GRBs and found that the pre- and postpeak emission periods were statistically similar, which seems to show the two emission periods are a common origin. They also found that 24% of GRBs had more than one isolated emission event, 11% of GRBs had at least one prepeak radiation event, and 15% of GRBs had at least one postpeak radiation event.

In fact, as shown by Charisi et al. (2015), it is also observed that a weak postpeak emission period occurs again after the end of the main burst, which is the postburst studied in this paper. There is a long period of quiescent time between the main burst and the postburst, just as there is between the precursor and the main burst. The study of GRB precursors and main bursts has yielded some very interesting results. However, the current paucity of studies of main bursts and postbursts in GRBs prompt us to wonder about the spectral properties of main bursts and postbursts. For example, can comparative studies of main bursts and postbursts provide evidence for the jet composition of GRBs? Do main bursts and postbursts come from the same origin and thus contribute to the activity of the central engine of GRBs? Therefore, we investigate two bright bursts with known redshift, GRB 160509A and GRB 130427A, which have both main bursts and postbursts, and will provide a deeper understanding of the radiative mechanisms as well as the spectral components of the GRB transients.

The paper is divided into six sections. In Sections 2 and 3, we introduce sample selection and analysis methods and the spectral models used in this paper. In Section 4, the analysis results are described. In Section 5, the photosphere radiation properties are derived, and in Sections 6 and 7 the discussion and conclusions are given.

2. Sample Selection and Analysis Methods

The data in this paper are from the Fermi satellite, which has two detectors, the Gamma-ray Burst Monitor (GBM) and the Large Area Telescope (LAT). Fourteen detectors on the GBM have 128 energy channels each, including 12 NaI detectors covering the effective channel range of 8–1000 keV, and two Bismuth Germanate (BGO detectors covering the effective channel range of 200 keV–40 MeV. GBM observations are stored in three file types: CTIME files, CSPEC files, and Time Tagged Event (TTE) files. Among the three data types, TTE data take up more memory and are generally used to record data only 30 s before and 300 s after the trigger. Compared to the first two file types, TTE files have the smallest time resolution (2μ s) and the best energy resolution and are suitable for analyzing the time-resolved spectra of GRBs. Therefore, we use TTE data for time-resolved spectral analysis.

GRB 160509A was detected on 2016 May 9 with trigger time $T_0 = 08{:}58{:}46.22$ UT and $T_{90} = 369.67$ s, redshift $z = 1.17$, its flux integrated over the entire GRB duration, Fluence $= 0.00017898$ erg cm^{-2}, according to the quicklook given by GRB. The NaI detectors chosen for the photographs are $n0$, $n1$, and $n3$, and the BGO detector is b0.

GRB 130427A was detected on 2013 April 27 with trigger time $T_0 = 07{:}47{:}06$ and $T_{90} = 138.242$ s, redshift $z = 0.34$, its flux integrated over the entire GRB duration, Fluence $= 0.002462$ erg cm^{-2}, selected based on the quicklook photos given by the GRB Na I detectors for na, $n6$, and $n9$, and BGO detectors for b1.

To track and study the spectral evolutions in the burst, detailed time-resolved spectral information is required. In this paper, we use the currently popular tool Multi-Mission Maximum Likelihood Framework (3ML; Vianello et al. 2015) software package to analyze the time-resolved spectral data of GRB 160509A and GRB 130427A (Yu et al. 2018). Traditional spectral analysis methods usually use the signal-to-noise ratio method to slice time. This method can ensure that there are enough photons to perform spectral analysis, but it may destroy the physical structure. Burgess (2014) compared four time slicing methods. He concluded that to obtain the most delicate time slicing while minimizing the influence of the mixed spectrum caused by the inherent spectral evolution, the Bayesian Blocks (BBlock) method should be used. BBlock has the following characteristics: (1) each bin obtained has a constant Poisson rate; (2) each bin has a different width and signal-to-noise ratio; (3) the algorithm is used to subdivide the GRB light curve for time bin selection; (4) the selection of time bin reflects the true variability of the data. However, the BBlock method cannot guarantee enough photons in each bin to perform accurate spectral fitting. Therefore, to ensure that there are enough photons to perform spectral fitting without destroying the physical structure, we first apply the BBlock method with alarm probability $p = 0.01$ (Scargle et al. 2013) to the TTE light curve of one of the brightest NaI detectors, and the other detectors follow the same time bin information. Then we calculate the statistical significance S (an appropriate measure of signal-to-noise ratio) for each bin and select bins with $S > 20$ (Vianello 2018).

Since the postburst of GRB 160509A occurs at 300–400 s, the CSPEC data are used and a new response matrix is produced with 3ML to fit the data. To better reveal the evolution of the time-resolved spectra, we choose spectra of significance, examine the spectral components of the emission period against the spectral data, and then check if there are thermal components. The ranges of the spectra we analyzed are shown in Figure 1. It can be seen that the quiescent time of GRB 160509A and GRB 130427A are 270 and 70 s, respectively.

3. Spectral Models

The study of the GRB spectra is important to understand the substance and can obtain a variety of information about GRBs. Although the GRBs light curve is very complex and takes a variety of forms, its spectrum is similar and most GRB spectra can be well fitted with the nonthermal empirical models. Therefore, we first consider the well-known empirical model, Band function (a smooth inflection power-law function) and the cutoff power-law function (CPL) (Band et al. 1993; Granot et al. 2011). The two empirical models used in this paper are as follows:

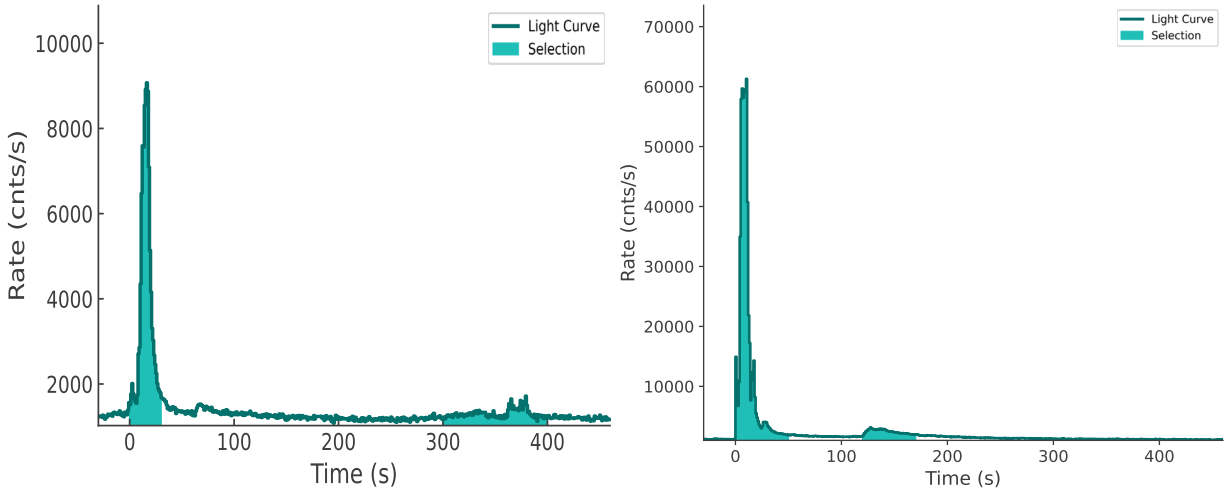

Figure 1. Light curves and spectral analysis ranges for GRB 160509A and GRB 130427A.

The Band function is

$$N_{Band}(E) = A\begin{cases}\left(\frac{E}{100\ \mathrm{keV}}\right)\exp\left(-\frac{E}{E_0}\right), & E < (\alpha-\beta)E_0 \\ \left(\frac{(\alpha-\beta)E_0}{100\ \mathrm{keV}}\right)^{\alpha-\beta}\exp(\beta-\alpha)\left(\frac{E}{100\ \mathrm{keV}}\right)^{\beta}, & E > (\alpha-\beta)E_0\end{cases} \quad (1)$$

where

$$E_p = (2+\alpha)E_0, \quad (2)$$

A is the normalization factor at 100 keV in units of photons s^{-1} cm^{-2} keV^{-1}, α is the low-energy spectral index, β is the high-energy spectral index, and E_p is the peak energy in units of keV in the observed νF_ν spectrum.

The CPL Function is

$$N_{\mathrm{CPL}}(E) = A\left(\frac{E}{E_{\mathrm{piv}}}\right)^{\alpha}\exp\left(-\frac{E}{E_0}\right), \quad (3)$$

where A is the normalization factor at 100 keV in units of photons s^{-1} cm^{-2} keV^{-1}, α is the low-energy spectral index and E_0 is the break energy in keV.

Some GRBs have additional thermal components, which are generally fitted by Planck blackbody (BB) function. The Planck function is given by

$$N_{\mathrm{BB}}(E) = A(t)\frac{E^2}{\exp[E/kT]-1}, \quad (4)$$

where E is the photon energy and k is Boltzmann's constant.

We first fit the time-resolved spectra using empirical models, Band and CPL, and the fitted results are filtered to find the best fit model by calculating the Bayesian Information Criterion (BIC) difference between the two model fits. To check for the presence of a thermal component in the spectra, an additional BB component is added to the selected best model to check for an improved fit statistic. We subtracted the fitted statistic obtained after the addition of the BB component from the fitted statistic obtained before the addition of the BB component. That is, we determine the value of Δ BIC ($\Delta\mathrm{BIC} = \mathrm{BIC}_{\mathrm{bestmodel}} - \mathrm{BIC}_{\mathrm{bestmodel+BB}}$); if the value of ΔBIC is greater than or equal to 10 then there is a blackbody component.

4. Analysis Results

4.1. Spectral Component Analysis

Using the above method and tool we can analyze the time-resolved spectral data of the two GRBs. For the main bursts we adopt the standard of $S > 20$ to select time slices since the photon number of the main bursts is very great. Due to the small photon number of the postburst, we adopt the same method of Li (2019), that is, the standard of $S > 20$ is not considered. In this way, GRB 160509A is divided into 39 time slices, of which 24 time slices are the main burst, and 17 meet the standard of $S > 20$. There are 15 time slices in the postburst. We first fit the spectra using Band and CPL models. For example, for the first time slice −1.0–0.91 s (see, Table 1), $\Delta BIC = \mathrm{BIC}_{\mathrm{Band}} - \mathrm{BIC}_{\mathrm{CPL}} = 11.17$, so the best model is the CPL model. Then, we select the thermal components. We use Band+BB and CPL+BB to fit the time-resolved spectra, and get $\Delta\mathrm{BIC}_{\mathrm{BB}} = \mathrm{BIC}_{\mathrm{Band+BB}} - \mathrm{BIC}_{\mathrm{CPL+BB}} = 10.724$, so CPL+BB is the best model. In the main burst, the best fitting model of 2 time slices is CPL, and the remaining 15 time slices is Band; after adding the BB component, the best fitting model of 2 time slices is CPL+BB, and the other time slices are Band+BB. In the postburst, the best fitting model of 15 time slices is CPL; after adding the BB component, the best fitting model of 11 time slices is CPL+BB, and the remaining 4 time slices is Band+BB. Similarly, GRB 130427A is divided into 93 time slices (see Table 2). The main burst has a total of 84 time slices, and there are 81 time slices with $S > 20$. Among them, the best model of 23 time slices is CPL, and the remaining 58 time slices is Band. After adding the BB component, the best model of 61 time slices is CPL+BB, and the remaining 20 time slices is Band+BB. There are a total of nine time slices in postburst, of which the best model for seven time slices is CPL, and the remaining two are Band. After adding the BB component, the best model with seven time slices is CPL+BB, and the other two time slices is Band+BB.

Figure 2 shows the evolution of ΔBIC over time for the main bursts and postbursts of GRB 160509A and GRB 130427A. For the GRB 160509A, the number of bins with a

Table 1
Time-resolved Spectral Fitting Result of GRB 160509A

$t_{start} - t_{end}$ (s) (1)	S (2)	Model (3)	α (4)	β (5)	E_p/E_c (keV) (6)	kT (keV) (7)	BIC (8)
−1.0−0.91	3	CPL	$-0.94^{+0.26}_{-0.26}$	⋯	$248.49^{+123.11}_{-130.29}$	⋯	4099.08
		Band	$-0.39^{+0.3}_{-0.25}$	$-2.24^{+0.16}_{-0.15}$	$113.61^{+20.0}_{-23.76}$	⋯	4110.25
		CPL+BB	$-0.9^{+0.34}_{-0.31}$	⋯	$180.5^{+123.11}_{-85.87}$	$24.86^{+7.93}_{-9.66}$	4090.53
		Band+BB	$-0.41^{+0.26}_{-0.26}$	$-2.32^{+0.31}_{-0.34}$	$81.55^{+42.07}_{-36.87}$	$31.63^{+7.78}_{-9.51}$	4101.25
0.91−4.21	11	CPL	$-0.91^{+0.09}_{-0.09}$	⋯	$487.97^{+122.85}_{-129.96}$	⋯	5247.79
		Band	$-0.56^{+0.35}_{-0.34}$	$-2.1^{+0.31}_{-0.38}$	$286.68^{+150.86}_{-132.72}$	⋯	5254.49
		CPL+BB	$-0.8^{+0.16}_{-0.15}$	⋯	$644.12^{+122.85}_{-200.92}$	$22.49^{+2.82}_{-2.85}$	5237.31
		Band+BB	$-0.81^{+0.13}_{-0.14}$	$-2.5^{+0.33}_{-0.34}$	$606.88^{+168.92}_{-169.84}$	$22.27^{+3.25}_{-3.12}$	5253.11
4.21−7.97	3	CPL	$-0.98^{+0.14}_{-0.14}$	⋯	$573.93^{+208.69}_{-236.77}$	⋯	5519.01
		Band	$-0.51^{+0.35}_{-0.36}$	$-1.8^{+0.15}_{-0.15}$	$205.72^{+95.9}_{-93.26}$	⋯	5523.74
		CPL+BB	$-0.91^{+0.16}_{-0.17}$	⋯	$612.19^{+208.69}_{-252.81}$	$19.55^{+5.09}_{-4.82}$	5516.26
		Band+BB	$-0.63^{+0.32}_{-0.32}$	$-1.88^{+0.22}_{-0.26}$	$283.16^{+164.93}_{-147.57}$	$18.28^{+5.54}_{-5.97}$	5515.26
7.97−8.35	10	CPL	$-0.74^{+0.13}_{-0.12}$	⋯	$384.41^{+110.68}_{-107.29}$	⋯	2160.65
		Band	$-0.65^{+0.15}_{-0.15}$	$-2.66^{+0.32}_{-0.32}$	$393.68^{+90.33}_{-92.09}$	⋯	2173.23
		CPL+BB	$-0.75^{+0.13}_{-0.13}$	⋯	$447.81^{+110.68}_{-141.22}$	$27.56^{+9.29}_{-9.47}$	2152.19
		Band+BB	$-0.69^{+0.14}_{-0.14}$	$-2.65^{+0.3}_{-0.3}$	$443.21^{+109.99}_{-105.91}$	$28.69^{+10.24}_{-11.33}$	2164.7
8.35−9.8	22	CPL	$-0.73^{+0.05}_{-0.05}$	⋯	$626.13^{+81.54}_{-81.99}$	⋯	4339.13
		Band	$-0.71^{+0.05}_{-0.05}$	$-2.81^{+0.27}_{-0.26}$	$743.16^{+67.49}_{-68.53}$	⋯	4348.87
		CPL+BB	$-0.5^{+0.12}_{-0.11}$	⋯	$614.29^{+81.54}_{-104.24}$	$25.25^{+2.07}_{-2.08}$	4317.51
		Band+BB	$-0.48^{+0.12}_{-0.11}$	$-2.87^{+0.23}_{-0.23}$	$837.23^{+84.6}_{-79.78}$	$24.82^{+1.99}_{-2.04}$	4332.95
9.8−10.31	23	CPL	$-0.8^{+0.05}_{-0.05}$	⋯	$752.47^{+137.92}_{-132.66}$	⋯	2755.88
		Band	$-0.73^{+0.07}_{-0.06}$	$-2.14^{+0.17}_{-0.17}$	$687.69^{+101.7}_{-107.12}$	⋯	2747.28
		CPL+BB	$-0.82^{+0.07}_{-0.07}$	⋯	$1048.08^{+137.92}_{-259.75}$	$32.72^{+5.44}_{-5.71}$	2746.83
		Band+BB	$-0.73^{+0.07}_{-0.07}$	$-2.2^{+0.18}_{-0.17}$	$838.07^{+152.52}_{-145.04}$	$29.13^{+6.17}_{-5.78}$	2742.99
10.31−10.92	35	CPL	$-0.68^{+0.04}_{-0.04}$	⋯	$447.62^{+44.54}_{-43.62}$	⋯	3187.42
		Band	$-0.59^{+0.06}_{-0.06}$	$-2.24^{+0.14}_{-0.14}$	$467.63^{+49.1}_{-48.0}$	⋯	3175.1
		CPL+BB	$-0.76^{+0.07}_{-0.07}$	⋯	$659.19^{+44.54}_{-131.74}$	$37.33^{+6.01}_{-6.14}$	3172.98
		Band+BB	$-0.65^{+0.07}_{-0.07}$	$-2.34^{+0.17}_{-0.17}$	$574.28^{+94.98}_{-94.7}$	$32.24^{+7.0}_{-6.66}$	3169.54
10.92−11.28	36	CPL	$-0.7^{+0.05}_{-0.05}$	⋯	$425.19^{+49.03}_{-48.13}$	⋯	2627.86
		Band	$-0.49^{+0.08}_{-0.08}$	$-1.93^{+0.07}_{-0.07}$	$336.42^{+39.25}_{-39.65}$	⋯	2584.0
		CPL+BB	$-0.95^{+0.07}_{-0.07}$	⋯	$1479.16^{+49.03}_{-452.07}$	$39.45^{+3.8}_{-3.69}$	2603.99
		Band+BB	$-0.57^{+0.11}_{-0.11}$	$-1.97^{+0.09}_{-0.09}$	$423.4^{+103.11}_{-98.2}$	$31.09^{+7.22}_{-9.05}$	2584.2
11.28−11.65	42	CPL	$-0.78^{+0.04}_{-0.04}$	⋯	$489.33^{+50.69}_{-51.59}$	⋯	2615.38
		Band	$-0.55^{+0.1}_{-0.09}$	$-1.94^{+0.09}_{-0.09}$	$344.63^{+55.93}_{-59.2}$	⋯	2579.87
		CPL+BB	$-0.81^{+0.05}_{-0.05}$	⋯	$806.25^{+50.69}_{-126.26}$	$28.97^{+2.14}_{-2.18}$	2581.23
		Band+BB	$-0.72^{+0.06}_{-0.06}$	$-2.15^{+0.12}_{-0.12}$	$638.99^{+90.11}_{-94.33}$	$27.23^{+2.4}_{-2.48}$	2570.79
11.65−13.01	73	CPL	$-0.86^{+0.02}_{-0.02}$	⋯	$627.85^{+32.67}_{-33.07}$	⋯	5084.51
		Band	$-0.76^{+0.02}_{-0.02}$	$-2.1^{+0.05}_{-0.05}$	$513.82^{+30.6}_{-30.73}$	⋯	4959.89
		CPL+BB	$-0.88^{+0.03}_{-0.03}$	⋯	$949.44^{+32.67}_{-85.2}$	$28.7^{+1.46}_{-1.45}$	4969.84
		Band+BB	$-0.78^{+0.03}_{-0.03}$	$-2.25^{+0.07}_{-0.07}$	$731.43^{+46.15}_{-48.13}$	$25.13^{+1.46}_{-1.5}$	4902.17
13.01−13.55	45	CPL	$-0.92^{+0.03}_{-0.03}$	⋯	$545.08^{+53.98}_{-56.02}$	⋯	3170.8
		Band	$-0.74^{+0.06}_{-0.07}$	$-1.95^{+0.07}_{-0.07}$	$340.28^{+45.45}_{-45.84}$	⋯	3130.36
		CPL+BB	$-1.0^{+0.04}_{-0.04}$	⋯	$969.82^{+53.98}_{-174.01}$	$28.78^{+2.6}_{-2.63}$	3144.62
		Band+BB	$-0.89^{+0.07}_{-0.07}$	$-2.11^{+0.12}_{-0.12}$	$567.09^{+116.12}_{-126.62}$	$27.25^{+3.06}_{-3.35}$	3129.66
13.55−13.82	47	CPL	$-0.83^{+0.03}_{-0.03}$	⋯	$480.99^{+45.93}_{-46.86}$	⋯	2361.1
		Band	$-0.72^{+0.05}_{-0.05}$	$-2.14^{+0.1}_{-0.1}$	$409.7^{+45.49}_{-44.75}$	⋯	2332.27
		CPL+BB	$-0.95^{+0.05}_{-0.05}$	⋯	$925.06^{+45.93}_{-188.34}$	$32.3^{+2.86}_{-2.84}$	2340.79
		Band+BB	$-0.84^{+0.06}_{-0.06}$	$-2.27^{+0.13}_{-0.13}$	$609.98^{+102.09}_{-102.89}$	$30.15^{+3.21}_{-3.25}$	2330.7
13.82−14.25	68	CPL	$-0.76^{+0.02}_{-0.03}$	⋯	$382.76^{+22.32}_{-23.32}$	⋯	3120.66
		Band	$-0.64^{+0.04}_{-0.04}$	$-2.24^{+0.08}_{-0.08}$	$356.64^{+23.18}_{-23.08}$	⋯	3077.2
		CPL+BB	$-0.83^{+0.04}_{-0.04}$	⋯	$579.07^{+22.32}_{-58.07}$	$28.55^{+1.78}_{-1.85}$	3073.34
		Band+BB	$-0.68^{+0.03}_{-0.11}$	$-2.4^{+0.19}_{-0.18}$	$469.63^{+95.95}_{-53.16}$	$42.6^{+-9.63}_{-17.33}$	3061.37
14.25−14.88	59	CPL	$-0.89^{+0.02}_{-0.03}$	⋯	$385.85^{+24.85}_{-25.13}$	⋯	3547.76
		Band	$-0.85^{+0.03}_{-0.03}$	$-2.57^{+0.16}_{-0.16}$	$374.87^{+23.14}_{-23.06}$	⋯	3543.97
		CPL+BB	$-0.91^{+0.03}_{-0.03}$	⋯	$509.14^{+24.85}_{-43.61}$	$22.99^{+1.45}_{-1.46}$	3518.61
		Band+BB	$-0.41^{+0.11}_{-0.06}$	$-2.25^{+0.13}_{-0.08}$	$156.41^{+-15.24}_{-36.55}$	$114.56^{+12.59}_{-1.03}$	3500.37

Table 1
(Continued)

$t_{start} - t_{end}$ (s) (1)	S (2)	Model (3)	α (4)	β (5)	E_p/E_c (keV) (6)	kT (keV) (7)	BIC (8)
14.88−16.66	82	CPL	$-0.9^{+0.01}_{-0.01}$	⋯	$394.68^{+15.35}_{-15.03}$	⋯	5563.36
		Band	$-0.81^{+0.02}_{-0.02}$	$-2.28^{+0.06}_{-0.07}$	$341.35^{+16.22}_{-16.77}$	⋯	5506.35
		CPL+BB	$-0.91^{+0.02}_{-0.02}$	⋯	$535.78^{+15.35}_{-32.32}$	$23.24^{+0.9}_{-0.92}$	5417.36
		Band+BB	$-0.37^{+0.05}_{-0.05}$	$-2.1^{+0.04}_{-0.04}$	$138.79^{+3.34}_{-6.73}$	$129.94^{+5.62}_{-4.56}$	5372.87
16.66−17.62	75	CPL	$-0.87^{+0.02}_{-0.02}$	⋯	$439.43^{+21.6}_{-21.76}$	⋯	4488.78
		Band	$-0.76^{+0.03}_{-0.03}$	$-2.13^{+0.05}_{-0.05}$	$364.75^{+20.95}_{-21.7}$	⋯	4391.6
		CPL+BB	$-0.94^{+0.03}_{-0.03}$	⋯	$636.88^{+21.6}_{-61.93}$	$29.73^{+2.08}_{-2.11}$	4443.5
		Band+BB	$-0.59^{+0.1}_{-0.22}$	$-1.99^{+0.08}_{-0.15}$	$230.86^{+197.7}_{-63.96}$	$102.41^{+21.39}_{-71.7}$	4362.55
17.62−18.57	56	CPL	$-1.0^{+0.02}_{-0.02}$	⋯	$758.01^{+65.31}_{-64.06}$	⋯	4448.24
		Band	$-0.82^{+0.04}_{-0.04}$	$-1.87^{+0.04}_{-0.04}$	$388.85^{+40.06}_{-40.82}$	⋯	4299.85
		CPL+BB	$-1.08^{+0.02}_{-0.02}$	⋯	$1621.9^{+65.31}_{-153.38}$	$28.66^{+1.65}_{-1.54}$	4361.1
		Band+BB	$-0.93^{+0.04}_{-0.04}$	$-1.97^{+0.06}_{-0.06}$	$654.04^{+96.78}_{-91.52}$	$24.84^{+1.54}_{-1.58}$	4284.79
18.57−18.99	39	CPL	$-0.97^{+0.04}_{-0.04}$	⋯	$460.05^{+51.48}_{-51.15}$	⋯	2932.43
		Band	$-0.86^{+0.05}_{-0.06}$	$-2.1^{+0.11}_{-0.11}$	$338.61^{+43.04}_{-42.39}$	⋯	2911.81
		CPL+BB	$-1.04^{+0.05}_{-0.05}$	⋯	$729.94^{+51.48}_{-152.03}$	$26.37^{+3.0}_{-2.99}$	2928.32
		Band+BB	$-0.85^{+0.18}_{-0.13}$	$-2.11^{+0.19}_{-0.16}$	$366.53^{+122.69}_{-207.37}$	$40.13^{+54.0}_{-19.01}$	2897.93
18.99−19.33	30	CPL	$-0.98^{+0.05}_{-0.05}$	⋯	$413.72^{+58.65}_{-59.55}$	⋯	2588.29
		Band	$-0.69^{+0.11}_{-0.11}$	$-1.86^{+0.06}_{-0.06}$	$203.52^{+36.43}_{-34.13}$	⋯	2556.92
		CPL+BB	$-1.13^{+0.08}_{-0.07}$	⋯	$958.01^{+58.65}_{-365.23}$	$27.58^{+3.03}_{-3.1}$	2588.12
		Band+BB	$-0.7^{+0.12}_{-0.12}$	$-1.84^{+0.07}_{-0.06}$	$202.38^{+42.92}_{-40.25}$	$33.28^{+19.56}_{-16.8}$	2549.51
19.33−20.13	31	CPL	$-1.25^{+0.02}_{-0.02}$	⋯	$1364.15^{+167.39}_{-175.65}$	⋯	4029.46
		Band	$-0.6^{+0.11}_{-0.11}$	$-1.76^{+0.03}_{-0.03}$	$148.67^{+17.81}_{-17.83}$	⋯	3905.12
		CPL+BB	$-1.24^{+0.03}_{-0.03}$	⋯	$1723.01^{+167.39}_{-121.34}$	$25.36^{+2.12}_{-1.94}$	3947.86
		Band+BB	$-0.64^{+0.1}_{-0.1}$	$-1.75^{+0.03}_{-0.03}$	$152.87^{+18.18}_{-18.69}$	$27.01^{+11.1}_{-10.44}$	3896.58
20.13−20.98	23	CPL	$-1.35^{+0.02}_{-0.02}$	⋯	$2353.48^{+386.43}_{-386.12}$	⋯	4050.58
		Band	$-0.85^{+0.11}_{-0.11}$	$-1.77^{+0.03}_{-0.03}$	$174.46^{+29.75}_{-30.42}$	⋯	4021.58
		CPL+BB	$-1.35^{+0.01}_{-0.01}$	⋯	$2600.89^{+386.43}_{-266.81}$	$29.81^{+3.57}_{-3.04}$	4019.62
		Band+BB	$-1.32^{+0.01}_{-0.05}$	$-2.59^{+0.16}_{-0.2}$	$1854.45^{+279.13}_{-182.34}$	$28.48^{+2.89}_{-2.45}$	4024.08
20.98−21.85	16	CPL	$-1.32^{+0.02}_{-0.02}$	⋯	$3226.23^{+545.95}_{-594.83}$	⋯	3956.11
		Band	$-1.01^{+0.06}_{-0.05}$	$-1.69^{+0.03}_{-0.03}$	$265.63^{+18.92}_{-18.8}$	⋯	3923.3
		CPL+BB	$-1.26^{+0.02}_{-0.02}$	⋯	$2026.78^{+545.95}_{-109.03}$	$60.0^{+2.25}_{-1.42}$	3962.63
		Band+BB	$-0.86^{+0.05}_{-0.05}$	$-1.64^{+0.02}_{-0.02}$	$162.91^{+21.96}_{-17.67}$	$32.06^{+2.4}_{-2.61}$	3909.38
21.85−23.24	13	CPL	$-1.33^{+0.03}_{-0.03}$	⋯	$6218.96^{+1243.98}_{-1260.65}$	⋯	4876.98
		Band	$-1.34^{+0.03}_{-0.03}$	$-2.67^{+0.31}_{-0.3}$	$4342.48^{+825.75}_{-804.09}$	⋯	4883.03
		CPL+BB	$-1.09^{+0.05}_{-0.06}$	⋯	$4099.66^{+1243.98}_{-577.05}$	$19.13^{+1.06}_{-1.1}$	4846.45
		Band+BB	$-1.27^{+0.03}_{-0.03}$	$-2.17^{+0.13}_{-0.14}$	$4410.79^{+856.48}_{-853.46}$	$22.8^{+2.34}_{-1.75}$	4857.9
23.24−24.0	7	CPL	$-1.17^{+0.01}_{-0.01}$	⋯	$1096.78^{+25.57}_{-32.08}$	⋯	3854.9
		Band	$-1.2^{+0.43}_{-0.14}$	$-1.92^{+0.29}_{-0.13}$	$3797.84^{+1856.47}_{-3637.39}$	⋯	3802.97
		CPL+BB	$-1.1^{+0.04}_{-0.04}$	⋯	$3946.17^{+25.57}_{-751.04}$	$29.23^{+0.94}_{-0.97}$	3785.07
		Band+BB	$-0.3^{+0.14}_{-0.24}$	$-1.62^{+0.02}_{-0.02}$	$119.45^{+20.02}_{-17.01}$	$15.66^{+3.93}_{-4.21}$	3781.22
300.0−310.27	5	CPL	$-0.54^{+0.27}_{-0.28}$	⋯	$517.41^{+216.01}_{-237.45}$	⋯	5994.72
		Band	$-0.27^{+0.3}_{-0.3}$	$-2.02^{+0.27}_{-0.27}$	$333.97^{+89.13}_{-100.13}$	⋯	6018.37
		CPL+BB	$-0.47^{+0.28}_{-0.27}$	⋯	$497.98^{+216.01}_{-207.96}$	$14.67^{+5.72}_{-5.76}$	5987.81
		Band+BB	$-0.14^{+0.27}_{-0.29}$	$-1.92^{+0.23}_{-0.24}$	$248.13^{+61.26}_{-66.04}$	$13.85^{+4.26}_{-4.28}$	6012.38
310.27−331.67	15	CPL	$-0.76^{+0.14}_{-0.14}$	⋯	$529.19^{+161.73}_{-160.86}$	⋯	7413.96
		Band	$-0.67^{+0.16}_{-0.17}$	$-2.23^{+0.3}_{-0.29}$	$489.92^{+117.55}_{-125.17}$	⋯	7432.19
		CPL+BB	$-0.63^{+0.18}_{-0.18}$	⋯	$489.68^{+161.73}_{-140.74}$	$17.71^{+5.14}_{-4.99}$	7407.24
		Band+BB	$-0.56^{+0.18}_{-0.19}$	$-2.14^{+0.26}_{-0.25}$	$448.03^{+105.62}_{-115.0}$	$15.73^{+4.39}_{-4.54}$	7427.38
331.67−340.94	18	CPL	$-0.72^{+0.14}_{-0.15}$	⋯	$360.72^{+109.79}_{-111.37}$	⋯	6146.86
		Band	$-0.55^{+0.25}_{-0.23}$	$-2.14^{+0.32}_{-0.32}$	$319.37^{+96.86}_{-103.62}$	⋯	6158.3
		CPL+BB	$-0.67^{+0.17}_{-0.17}$	⋯	$381.3^{+109.79}_{-120.25}$	$19.4^{+6.98}_{-7.12}$	6138.67
		Band+BB	$-0.52^{+0.24}_{-0.24}$	$-2.17^{+0.31}_{-0.33}$	$341.51^{+101.05}_{-106.29}$	$16.88^{+6.28}_{-6.27}$	6151.06
340.94−345.17	7	CPL	$-0.3^{+0.29}_{-0.3}$	⋯	$238.58^{+84.27}_{-91.82}$	⋯	4726.03
		Band	$-0.17^{+0.33}_{-0.32}$	$-2.34^{+0.3}_{-0.31}$	$284.47^{+69.53}_{-71.92}$	⋯	4746.05
		CPL+BB	$-0.4^{+0.31}_{-0.31}$	⋯	$272.61^{+84.27}_{-129.44}$	$29.99^{+20.97}_{-18.54}$	4713.53

Table 1
(Continued)

$t_{start} - t_{end}$ (s) (1)	S (2)	Model (3)	α (4)	β (5)	E_p/E_c (keV) (6)	kT (keV) (7)	BIC (8)
		Band+BB	$-0.15^{+0.27}_{-0.27}$	$-2.23^{+0.37}_{-0.36}$	$78.67^{+59.95}_{-55.43}$	$49.07^{+10.5}_{-10.8}$	4729.68
345.17−362.26	4	CPL	$-0.6^{+0.28}_{-0.28}$	⋯	$486.53^{+253.51}_{-247.95}$	⋯	6906.42
		Band	$-0.11^{+0.32}_{-0.32}$	$-2.11^{+0.32}_{-0.31}$	$200.1^{+64.38}_{-70.13}$	⋯	6931.22
		CPL+BB	$-0.55^{+0.26}_{-0.26}$	⋯	$474.57^{+253.51}_{-206.26}$	$15.68^{+6.61}_{-6.24}$	6899.3
		Band+BB	$-0.12^{+0.27}_{-0.3}$	$-2.15^{+0.36}_{-0.35}$	$138.18^{+78.63}_{-99.36}$	$18.32^{+18.32}_{-9.67}$	6925.51
362.26−365.06	24	CPL	$-0.78^{+0.11}_{-0.11}$	⋯	$336.04^{+66.47}_{-75.02}$	⋯	4570.79
		Band	$-0.77^{+0.11}_{-0.11}$	$-2.52^{+0.35}_{-0.33}$	$384.16^{+65.27}_{-65.01}$	⋯	4584.54
		CPL+BB	$-0.7^{+0.14}_{-0.14}$	⋯	$333.4^{+66.47}_{-72.84}$	$17.12^{+4.52}_{-4.57}$	4578.21
		Band+BB	$-0.1^{+0.27}_{-0.25}$	$-2.37^{+0.32}_{-0.3}$	$85.38^{+-1.08}_{-22.32}$	$88.55^{+8.04}_{-3.81}$	4568.91
365.06−365.36	15	CPL	$-1.04^{+0.13}_{-0.13}$	⋯	$850.7^{+346.49}_{-382.11}$	⋯	1098.32
		Band	$-0.88^{+0.3}_{-0.26}$	$-2.12^{+0.37}_{-0.41}$	$492.65^{+277.71}_{-308.05}$	⋯	1103.81
		CPL+BB	$-1.05^{+0.12}_{-0.13}$	⋯	$949.33^{+346.49}_{-432.61}$	$24.83^{+8.69}_{-8.83}$	1089.86
		Band+BB	$-0.93^{+0.23}_{-0.22}$	$-2.14^{+0.37}_{-0.36}$	$542.47^{+298.0}_{-325.2}$	$25.43^{+9.34}_{-9.83}$	1097.89
365.36−373.44	27	CPL	$-0.9^{+0.11}_{-0.11}$	⋯	$285.95^{+69.53}_{-68.16}$	⋯	6328.71
		Band	$-0.56^{+0.35}_{-0.31}$	$-2.06^{+0.27}_{-0.31}$	$183.67^{+78.87}_{-77.0}$	⋯	6336.89
		CPL+BB	$-0.82^{+0.16}_{-0.16}$	⋯	$308.39^{+69.53}_{-80.46}$	$16.23^{+3.76}_{-3.54}$	6336.26
		Band+BB	$-0.59^{+0.36}_{-0.3}$	$-2.25^{+0.36}_{-0.35}$	$213.97^{+110.83}_{-140.6}$	$27.94^{+34.13}_{-15.1}$	6328.98
373.44−375.53	28	CPL	$-0.92^{+0.14}_{-0.14}$	⋯	$202.62^{+53.05}_{-56.98}$	⋯	4244.97
		Band	$-0.41^{+0.26}_{-0.25}$	$-2.15^{+0.16}_{-0.15}$	$115.8^{+22.34}_{-23.16}$	⋯	4245.54
		CPL+BB	$-1.03^{+0.14}_{-0.14}$	⋯	$342.98^{+53.05}_{-147.39}$	$20.57^{+3.91}_{-3.91}$	4251.33
		Band+BB	$-0.45^{+0.24}_{-0.23}$	$-2.12^{+0.16}_{-0.16}$	$114.4^{+23.34}_{-25.88}$	$23.66^{+10.54}_{-10.17}$	4238.39
375.53−376.68	10	CPL	$-0.67^{+0.3}_{-0.29}$	⋯	$169.22^{+53.02}_{-80.35}$	⋯	2748.89
		Band	$-0.4^{+0.31}_{-0.33}$	$-2.26^{+0.35}_{-0.35}$	$135.57^{+31.22}_{-33.04}$	⋯	2756.67
		CPL+BB	$-0.86^{+0.32}_{-0.35}$	⋯	$239.93^{+53.02}_{-148.96}$	$29.8^{+7.57}_{-7.37}$	2739.25
		Band+BB	$-0.44^{+0.29}_{-0.31}$	$-2.18^{+0.33}_{-0.3}$	$114.12^{+39.01}_{-49.78}$	$27.88^{+8.71}_{-9.67}$	2747.58
376.68−379.15	25	CPL	$-0.93^{+0.13}_{-0.13}$	⋯	$212.66^{+54.58}_{-55.57}$	⋯	4337.75
		Band	$-0.61^{+0.26}_{-0.24}$	$-2.26^{+0.27}_{-0.28}$	$144.62^{+34.27}_{-36.21}$	⋯	4344.52
		CPL+BB	$-0.96^{+0.15}_{-0.14}$	⋯	$244.54^{+54.58}_{-74.65}$	$20.95^{+6.8}_{-6.75}$	4329.87
		Band+BB	$-0.65^{+0.25}_{-0.26}$	$-2.23^{+0.28}_{-0.31}$	$147.11^{+47.48}_{-46.75}$	$22.87^{+10.01}_{-9.28}$	4336.88
379.15−380.35	33	CPL	$-0.61^{+0.14}_{-0.14}$	⋯	$133.92^{+25.03}_{-25.69}$	⋯	3606.02
		Band	$-0.3^{+0.21}_{-0.22}$	$-2.42^{+0.23}_{-0.24}$	$135.05^{+17.76}_{-18.31}$	⋯	3612.32
		CPL+BB	$-0.67^{+0.15}_{-0.14}$	⋯	$158.93^{+25.03}_{-39.24}$	$23.63^{+4.95}_{-6.71}$	3610.52
		Band+BB	$-0.34^{+0.21}_{-0.22}$	$-2.39^{+0.24}_{-0.23}$	$133.89^{+26.89}_{-28.7}$	$28.33^{+16.06}_{-12.27}$	3604.79
380.35−381.74	17	CPL	$-0.8^{+0.28}_{-0.28}$	⋯	$100.15^{+33.78}_{-40.36}$	⋯	3226.91
		Band	$-0.44^{+0.3}_{-0.24}$	$-2.4^{+0.26}_{-0.25}$	$76.16^{+13.49}_{-15.01}$	⋯	3232.99
		CPL+BB	$-0.94^{+0.28}_{-0.27}$	⋯	$116.54^{+33.78}_{-50.69}$	$20.7^{+7.01}_{-6.86}$	3219.02
		Band+BB	$-0.48^{+0.31}_{-0.29}$	$-2.24^{+0.19}_{-0.19}$	$68.96^{+13.66}_{-15.02}$	$21.73^{+6.84}_{-6.54}$	3225.06
381.74−384.92	10	CPL	$-0.91^{+0.27}_{-0.27}$	⋯	$328.76^{+170.85}_{-197.53}$	⋯	4205.88
		Band	$-0.31^{+0.28}_{-0.3}$	$-2.01^{+0.27}_{-0.29}$	$98.64^{+32.9}_{-34.45}$	⋯	4215.59
		CPL+BB	$-0.89^{+0.28}_{-0.27}$	⋯	$336.4^{+170.85}_{-214.19}$	$21.11^{+7.36}_{-7.51}$	4198.34
		Band+BB	$-0.27^{+0.3}_{-0.31}$	$-1.97^{+0.24}_{-0.24}$	$87.19^{+35.52}_{-34.7}$	$20.49^{+9.39}_{-8.37}$	4208.39
384.92−390.0	3	CPL	$-0.8^{+0.38}_{-0.44}$	⋯	$176.35^{+107.85}_{-134.95}$	⋯	4818.5
		Band	$-0.15^{+0.28}_{-0.28}$	$-2.19^{+0.33}_{-0.42}$	$27.33^{+13.79}_{-14.12}$	⋯	4835.98
		CPL+BB	$-0.76^{+0.38}_{-0.37}$	⋯	$184.52^{+107.85}_{-143.7}$	$13.42^{+4.18}_{-4.21}$	4811.62
		Band+BB	$-0.12^{+0.29}_{-0.29}$	$-2.23^{+0.35}_{-0.34}$	$24.51^{+9.55}_{-10.72}$	$14.61^{+5.45}_{-5.43}$	4828.97

significant thermal component in the main burst is nine, 53% of the total (9/17), and only one bin is detected in the postburst. For GRB 130427A, the number of bins with a significant thermal component in the main burst is 73.90% of the total (73/81). The postburst also has only one bin with a detectable thermal component. As can be seen, both bursts show a severe weakening of the thermal component from the main burst to the postburst.

4.2. Parameter Evolution

Previous studies have shown that there are two main evolution modes of spectral parameter: a "hard-to-soft" mode, which shows that the decrease and increase in spectral parameters are independent of the rise and decay of the flux; and a flux "tracking" mode, indicating that the parameters are correlated with the rise and fall of the flux. Li (2019) and

Table 2
Time-resolved Spectral Fitting Result of GRB 130427A

$t_{start} - t_{end}$ (s)	S	Model	α	β	E_p/E_c (keV)	kT (keV)	BIC
(1)	(2)	(3)	(4)	(5)	(6)	(7)	(8)
0.0−0.07	17	CPL	$-0.39^{+0.09}_{-0.09}$	⋯	$1049.31^{+150.34}_{-161.1}$	⋯	239.81
		Band	$-0.4^{+0.08}_{-0.08}$	$-2.81^{+0.3}_{-0.29}$	$1627.85^{+203.91}_{-206.88}$	⋯	256.7
		CPL+BB	$-0.35^{+0.09}_{-0.1}$	⋯	$1027.97^{+150.34}_{-148.03}$	$30.63^{+14.24}_{-14.14}$	231.26
		Band+BB	$-0.37^{+0.1}_{-0.1}$	$-2.8^{+0.29}_{-0.29}$	$1634.88^{+199.82}_{-192.72}$	$29.98^{+14.08}_{-13.39}$	248.58
0.07−0.16	34	CPL	$-0.3^{+0.06}_{-0.06}$	⋯	$675.15^{+65.52}_{-65.98}$	⋯	450.47
		Band	$-0.24^{+0.07}_{-0.07}$	$-2.8^{+0.23}_{-0.22}$	$1032.43^{+87.1}_{-87.67}$	⋯	459.51
		CPL+BB	$-0.33^{+0.09}_{-0.09}$	⋯	$746.65^{+65.52}_{-119.37}$	$65.09^{+55.45}_{-42.95}$	442.81
		Band+BB	$-0.26^{+0.1}_{-0.08}$	$-2.8^{+0.23}_{-0.22}$	$1085.06^{+110.65}_{-121.73}$	$51.75^{+44.48}_{-33.27}$	451.59
0.16−0.22	38	CPL	$-0.17^{+0.06}_{-0.07}$	⋯	$469.33^{+42.93}_{-44.39}$	⋯	324.49
		Band	$-0.13^{+0.07}_{-0.07}$	$-2.95^{+0.22}_{-0.22}$	$793.12^{+54.47}_{-53.29}$	⋯	337.93
		CPL+BB	$-0.22^{+0.1}_{-0.1}$	⋯	$530.44^{+42.93}_{-82.43}$	$68.58^{+35.19}_{-39.03}$	315.54
		Band+BB	$-0.17^{+0.1}_{-0.1}$	$-2.9^{+0.24}_{-0.27}$	$823.21^{+97.4}_{-71.69}$	$72.37^{+43.27}_{-46.81}$	329.31
0.22−0.36	75	CPL	$-0.34^{+0.03}_{-0.03}$	⋯	$407.92^{+21.46}_{-21.47}$	⋯	914.11
		Band	$-0.31^{+0.04}_{-0.03}$	$-3.26^{+0.22}_{-0.22}$	$642.13^{+23.78}_{-25.89}$	⋯	935.26
		CPL+BB	$-0.35^{+0.04}_{-0.04}$	⋯	$418.81^{+21.46}_{-26.36}$	$45.17^{+19.03}_{-20.48}$	905.82
		Band+BB	$-0.3^{+0.04}_{-0.05}$	$-3.14^{+0.37}_{-0.32}$	$596.46^{+84.66}_{-184.64}$	$66.83^{+102.98}_{-43.92}$	919.31
0.36−0.78	152	CPL	$-0.66^{+0.02}_{-0.02}$	⋯	$364.93^{+11.3}_{-11.69}$	⋯	2408.1
		Band	$-0.64^{+0.02}_{-0.02}$	$-3.29^{+0.2}_{-0.2}$	$472.66^{+12.74}_{-12.69}$	⋯	2425.29
		CPL+BB	$-0.42^{+0.04}_{-0.03}$	⋯	$152.28^{+11.3}_{-14.37}$	$187.85^{+8.11}_{-4.15}$	2370.64
		Band+BB	$-0.44^{+0.03}_{-0.03}$	$-2.79^{+0.15}_{-0.16}$	$240.95^{+13.96}_{-13.82}$	$171.39^{+6.46}_{-6.89}$	2381.15
0.78−0.95	88	CPL	$-0.69^{+0.03}_{-0.03}$	⋯	$224.69^{+12.03}_{-12.1}$	⋯	1177.8
		Band	$-0.65^{+0.04}_{-0.04}$	$-3.18^{+0.24}_{-0.23}$	$276.65^{+11.78}_{-12.29}$	⋯	1201.41
		CPL+BB	$-0.67^{+0.08}_{-0.06}$	⋯	$211.02^{+12.03}_{-62.05}$	$53.15^{+68.62}_{-30.9}$	1169.69
		Band+BB	$-0.6^{+0.08}_{-0.08}$	$-3.09^{+0.25}_{-0.25}$	$228.19^{+54.44}_{-51.85}$	$79.34^{+38.95}_{-51.61}$	1190.85
0.95−1.44	113	CPL	$-0.72^{+0.03}_{-0.03}$	⋯	$169.41^{+7.08}_{-7.04}$	⋯	2224.77
		Band	$-0.65^{+0.03}_{-0.03}$	$-2.99^{+0.15}_{-0.15}$	$196.85^{+6.9}_{-6.71}$	⋯	2232.05
		CPL+BB	$-0.51^{+0.05}_{-0.05}$	⋯	$95.16^{+7.08}_{-8.99}$	$113.87^{+8.77}_{-9.44}$	2198.37
		Band+BB	$-0.54^{+0.06}_{-0.06}$	$-3.09^{+0.23}_{-0.24}$	$147.63^{+12.11}_{-14.61}$	$93.0^{+13.38}_{-8.21}$	2220.21
1.44−2.13	117	CPL	$-0.65^{+0.03}_{-0.03}$	⋯	$113.69^{+4.34}_{-4.24}$	⋯	2581.9
		Band	$-0.57^{+0.04}_{-0.04}$	$-3.05^{+0.16}_{-0.16}$	$140.44^{+4.27}_{-4.22}$	⋯	2588.78
		CPL+BB	$-0.41^{+0.07}_{-0.07}$	⋯	$67.82^{+4.34}_{-7.8}$	$82.96^{+8.04}_{-7.74}$	2555.35
		Band+BB	$-0.42^{+0.07}_{-0.07}$	$-2.99^{+0.19}_{-0.19}$	$105.84^{+9.01}_{-9.3}$	$63.43^{+6.63}_{-5.84}$	2574.14
2.13−2.4	55	CPL	$-0.64^{+0.06}_{-0.06}$	⋯	$92.56^{+6.97}_{-7.28}$	⋯	1282.92
		Band	$-0.5^{+0.09}_{-0.09}$	$-2.86^{+0.21}_{-0.21}$	$110.67^{+6.71}_{-6.73}$	⋯	1293.29
		CPL+BB	$-0.5^{+0.16}_{-0.16}$	⋯	$70.57^{+6.97}_{-17.92}$	$56.04^{+19.33}_{-30.87}$	1273.41
		Band+BB	$-0.46^{+0.11}_{-0.11}$	$-2.83^{+0.19}_{-0.19}$	$101.08^{+11.29}_{-11.54}$	$40.56^{+15.38}_{-17.59}$	1287.57
2.4−2.85	55	CPL	$-0.69^{+0.07}_{-0.07}$	⋯	$77.91^{+5.94}_{-6.06}$	⋯	1862.95
		Band	$-0.54^{+0.08}_{-0.08}$	$-2.99^{+0.17}_{-0.17}$	$91.22^{+4.27}_{-4.07}$	⋯	1873.58
		CPL+BB	$-0.5^{+0.13}_{-0.15}$	⋯	$55.53^{+5.94}_{-10.38}$	$55.1^{+12.49}_{-9.5}$	1851.16
		Band+BB	$-0.53^{+0.09}_{-0.09}$	$-3.02^{+0.19}_{-0.19}$	$86.66^{+5.69}_{-6.39}$	$35.58^{+15.08}_{-16.12}$	1866.49
2.85−3.24	65	CPL	$-0.65^{+0.06}_{-0.06}$	⋯	$85.11^{+5.59}_{-5.45}$	⋯	1773.13
		Band	$-0.57^{+0.07}_{-0.07}$	$-3.05^{+0.19}_{-0.19}$	$105.91^{+4.14}_{-4.22}$	⋯	1789.42
		CPL+BB	$-0.59^{+0.11}_{-0.1}$	⋯	$74.52^{+5.59}_{-16.17}$	$43.39^{+21.67}_{-24.03}$	1764.27
		Band+BB	$-0.55^{+0.09}_{-0.09}$	$-3.05^{+0.23}_{-0.22}$	$99.35^{+9.6}_{-10.73}$	$36.01^{+12.61}_{-15.2}$	1782.4
3.24−3.58	81	CPL	$-0.73^{+0.04}_{-0.04}$	⋯	$140.45^{+8.04}_{-7.91}$	⋯	1724.59
		Band	$-0.53^{+0.06}_{-0.06}$	$-2.53^{+0.11}_{-0.11}$	$142.71^{+8.17}_{-8.1}$	⋯	1711.32
		CPL+BB	$-0.34^{+0.08}_{-0.09}$	⋯	$63.37^{+8.04}_{-7.3}$	$96.9^{+9.36}_{-8.85}$	1689.07
		Band+BB	$-0.4^{+0.09}_{-0.09}$	$-2.6^{+0.16}_{-0.17}$	$112.84^{+10.71}_{-11.16}$	$71.44^{+12.58}_{-9.3}$	1698.67
3.58−3.81	81	CPL	$-0.71^{+0.04}_{-0.04}$	⋯	$166.04^{+10.16}_{-10.4}$	⋯	1367.17
		Band	$-0.62^{+0.06}_{-0.06}$	$-2.8^{+0.18}_{-0.17}$	$189.68^{+10.78}_{-10.48}$	⋯	1373.0
		CPL+BB	$-0.49^{+0.08}_{-0.07}$	⋯	$95.79^{+10.16}_{-17.22}$	$101.81^{+16.2}_{-7.88}$	1351.31
		Band+BB	$-0.55^{+0.1}_{-0.1}$	$-2.74^{+0.2}_{-0.2}$	$157.25^{+33.97}_{-28.26}$	$65.15^{+23.37}_{-35.13}$	1362.82
3.81−4.04	101	CPL	$-0.74^{+0.03}_{-0.03}$	⋯	$288.16^{+15.08}_{-14.44}$	⋯	1567.64
		Band	$-0.62^{+0.04}_{-0.04}$	$-2.45^{+0.1}_{-0.1}$	$286.62^{+17.1}_{-16.83}$	⋯	1548.95
		CPL+BB	$-0.49^{+0.12}_{-0.32}$	⋯	$167.57^{+15.08}_{-66.35}$	$131.37^{+29.22}_{-97.37}$	1528.03
		Band+BB	$-0.47^{+0.06}_{-0.06}$	$-2.44^{+0.12}_{-0.12}$	$196.87^{+15.04}_{-20.11}$	$130.66^{+15.99}_{-10.65}$	1530.65

Table 2
(Continued)

$t_{start} - t_{end}$ (s) (1)	S (2)	Model (3)	α (4)	β (5)	E_p/E_c (keV) (6)	kT (keV) (7)	BIC (8)
4.04−4.33	151	CPL	$-0.59^{+0.02}_{-0.02}$	⋯	$309.44^{+9.83}_{-9.72}$	⋯	2049.31
		Band	$-0.54^{+0.02}_{-0.02}$	$-3.07^{+0.17}_{-0.16}$	$403.79^{+11.86}_{-12.19}$	⋯	2063.64
		CPL+BB	$-0.61^{+0.02}_{-0.03}$	⋯	$337.77^{+9.83}_{-15.18}$	$34.28^{+4.77}_{-5.02}$	2041.04
		Band+BB	$-0.38^{+0.03}_{-0.04}$	$-2.98^{+0.21}_{-0.22}$	$249.11^{+16.03}_{-16.54}$	$170.64^{+10.72}_{-11.32}$	2027.89
4.33−4.49	132	CPL	$-0.53^{+0.02}_{-0.02}$	⋯	$328.08^{+11.63}_{-11.45}$	⋯	1252.5
		Band	$-0.5^{+0.03}_{-0.03}$	$-3.13^{+0.2}_{-0.2}$	$449.79^{+16.15}_{-16.73}$	⋯	1267.31
		CPL+BB	$-0.58^{+0.03}_{-0.03}$	⋯	$379.96^{+11.63}_{-21.9}$	$39.84^{+4.47}_{-4.52}$	1245.32
		Band+BB	$-0.31^{+0.05}_{-0.04}$	$-2.84^{+0.18}_{-0.17}$	$263.4^{+22.32}_{-22.07}$	$176.1^{+12.13}_{-11.56}$	1237.07
4.49−4.73	181	CPL	$-0.52^{+0.02}_{-0.02}$	⋯	$338.99^{+9.06}_{-9.44}$	⋯	1960.87
		Band	$-0.43^{+0.02}_{-0.02}$	$-2.84^{+0.09}_{-0.09}$	$436.62^{+11.77}_{-11.42}$	⋯	1921.32
		CPL+BB	$-0.29^{+0.02}_{-0.02}$	⋯	$177.52^{+9.06}_{-7.42}$	$257.51^{+9.51}_{-8.3}$	1860.72
		Band+BB	$-0.31^{+0.04}_{-0.01}$	$-2.7^{+0.1}_{-0.04}$	$306.03^{+-6.1}_{-25.4}$	$176.9^{+13.17}_{2.37}$	1882.94
4.73−4.91	191	CPL	$-0.5^{+0.01}_{-0.01}$	⋯	$417.17^{+10.77}_{-10.72}$	⋯	1766.63
		Band	$-0.43^{+0.02}_{-0.02}$	$-2.9^{+0.09}_{-0.09}$	$551.86^{+14.1}_{-13.91}$	⋯	1713.37
		CPL+BB	$-0.58^{+0.02}_{-0.02}$	⋯	$550.68^{+10.77}_{-25.07}$	$49.06^{+2.91}_{-2.82}$	1673.5
		Band+BB	$-0.26^{+0.05}_{-0.02}$	$-2.71^{+0.14}_{-0.09}$	$360.65^{+-0.98}_{-43.93}$	$223.13^{+26.58}_{-3.09}$	1651.98
4.91−5.12	222	CPL	$-0.46^{+0.01}_{-0.01}$	⋯	$565.98^{+12.31}_{-12.69}$	⋯	2173.68
		Band	$-0.39^{+0.02}_{-0.02}$	$-3.04^{+0.09}_{-0.09}$	$762.69^{+17.26}_{-17.4}$	⋯	2117.0
		CPL+BB	$-0.53^{+0.02}_{-0.02}$	⋯	$727.37^{+12.31}_{-25.2}$	$62.23^{+3.3}_{-3.22}$	2013.49
		Band+BB	$-0.49^{+0.02}_{-0.02}$	$-3.68^{+0.19}_{-0.17}$	$986.02^{+32.47}_{-32.14}$	$58.17^{+3.52}_{-3.45}$	2044.34
5.12−5.48	293	CPL	$-0.36^{+0.01}_{-0.01}$	⋯	$405.26^{+5.94}_{-5.97}$	⋯	3118.07
		Band	$-0.29^{+0.01}_{-0.01}$	$-3.23^{+0.08}_{-0.07}$	$602.4^{+8.47}_{-8.83}$	⋯	3031.83
		CPL+BB	$-0.44^{+0.02}_{-0.02}$	⋯	$520.47^{+5.94}_{-14.15}$	$58.04^{+2.32}_{-2.31}$	2887.77
		Band+BB	$-0.14^{+0.01}_{-0.01}$	$-3.36^{+0.1}_{-0.11}$	$411.37^{+8.98}_{-8.45}$	$294.2^{+6.44}_{-6.12}$	2888.47
5.48−5.75	273	CPL	$-0.48^{+0.01}_{-0.01}$	⋯	$337.64^{+6.22}_{-6.37}$	⋯	2645.63
		Band	$-0.36^{+0.02}_{-0.02}$	$-2.74^{+0.06}_{-0.06}$	$424.38^{+9.15}_{-8.76}$	⋯	2461.91
		CPL+BB	$-0.2^{+0.02}_{-0.02}$	⋯	$166.19^{+6.22}_{-5.71}$	$269.21^{+6.35}_{-5.9}$	2329.81
		Band+BB	$-0.19^{+0.02}_{-0.02}$	$-2.75^{+0.07}_{-0.08}$	$289.96^{+9.55}_{-9.61}$	$218.04^{+9.64}_{-9.44}$	2320.88
5.75−5.84	146	CPL	$-0.6^{+0.02}_{-0.02}$	⋯	$345.75^{+13.04}_{-13.06}$	⋯	984.65
		Band	$-0.52^{+0.03}_{-0.03}$	$-2.77^{+0.12}_{-0.12}$	$420.74^{+17.41}_{-17.52}$	⋯	964.35
		CPL+BB	$-0.3^{+0.05}_{-0.04}$	⋯	$146.46^{+13.04}_{-18.29}$	$210.93^{+15.77}_{-11.13}$	926.07
		Band+BB	$-0.24^{+0.06}_{-0.06}$	$-2.42^{+0.1}_{-0.09}$	$215.74^{+19.71}_{-19.34}$	$163.17^{+10.39}_{-10.91}$	922.99
5.84−6.03	183	CPL	$-0.67^{+0.02}_{-0.02}$	⋯	$332.98^{+10.4}_{-10.55}$	⋯	1809.07
		Band	$-0.5^{+0.03}_{-0.03}$	$-2.47^{+0.06}_{-0.06}$	$324.81^{+11.62}_{-11.67}$	⋯	1705.57
		CPL+BB	$-0.35^{+0.02}_{-0.03}$	⋯	$139.72^{+10.4}_{-5.63}$	$238.11^{+7.45}_{-7.83}$	1607.19
		Band+BB	$-0.35^{+0.03}_{-0.03}$	$-2.77^{+0.12}_{-0.12}$	$234.34^{+8.87}_{-8.47}$	$216.96^{+12.99}_{-13.04}$	1623.11
6.03−6.14	175	CPL	$-0.69^{+0.01}_{-0.01}$	⋯	$710.91^{+22.29}_{-22.07}$	⋯	1317.74
		Band	$-0.64^{+0.02}_{-0.02}$	$-2.93^{+0.12}_{-0.12}$	$814.37^{+27.51}_{-28.32}$	⋯	1302.64
		CPL+BB	$-0.75^{+0.02}_{-0.02}$	⋯	$914.93^{+22.29}_{-42.11}$	$53.6^{+3.18}_{-3.12}$	1238.06
		Band+BB	$-0.72^{+0.02}_{-0.02}$	$-3.41^{+0.19}_{-0.19}$	$1060.57^{+45.06}_{-43.7}$	$52.07^{+3.34}_{-3.33}$	1261.46
6.14−6.47	278	CPL	$-0.52^{+0.01}_{-0.01}$	⋯	$590.95^{+10.05}_{-10.32}$	⋯	3076.58
		Band	$-0.43^{+0.01}_{-0.01}$	$-2.82^{+0.06}_{-0.06}$	$730.04^{+13.28}_{-13.92}$	⋯	2847.28
		CPL+BB	$-0.59^{+0.01}_{-0.01}$	⋯	$802.22^{+10.05}_{-23.13}$	$58.81^{+2.14}_{-2.12}$	2724.02
		Band+BB	$-0.52^{+0.02}_{-0.02}$	$-3.32^{+0.11}_{-0.11}$	$973.66^{+28.24}_{-29.52}$	$52.48^{+2.48}_{-2.46}$	2701.67
6.47−6.65	227	CPL	$-0.44^{+0.01}_{-0.01}$	⋯	$272.8^{+5.56}_{-5.76}$	⋯	2100.27
		Band	$-0.23^{+0.02}_{-0.02}$	$-2.58^{+0.04}_{-0.04}$	$323.93^{+7.57}_{-7.53}$	⋯	1884.36
		CPL+BB	$-0.06^{+0.03}_{-0.03}$	⋯	$125.84^{+5.56}_{-5.42}$	$239.2^{+9.47}_{-9.28}$	1742.19
		Band+BB	$-0.05^{+0.03}_{-0.03}$	$-2.85^{+0.11}_{-0.12}$	$240.99^{+8.61}_{-8.42}$	$204.92^{+12.5}_{-12.71}$	1760.3
6.65−7.17	339	CPL	$-0.55^{+0.01}_{-0.01}$	⋯	$682.1^{+9.28}_{-9.53}$	⋯	4107.82
		Band	$-0.5^{+0.01}_{-0.01}$	$-3.11^{+0.07}_{-0.07}$	$887.61^{+13.08}_{-12.57}$	⋯	3935.23
		CPL+BB	$-0.57^{+0.01}_{-0.01}$	⋯	$822.63^{+9.28}_{-16.81}$	$51.54^{+1.74}_{-1.68}$	3659.33
		Band+BB	$-0.53^{+0.01}_{-0.01}$	$-3.63^{+0.11}_{-0.11}$	$1096.24^{+18.79}_{-18.91}$	$48.26^{+1.71}_{-1.64}$	3632.46
7.17−7.23	131	CPL	$-0.42^{+0.02}_{-0.02}$	⋯	$422.9^{+16.53}_{-15.42}$	⋯	695.48
		Band	$-0.36^{+0.03}_{-0.03}$	$-3.14^{+0.16}_{-0.16}$	$602.44^{+20.21}_{-19.94}$	⋯	703.49
		CPL+BB	$-0.35^{+0.22}_{-0.15}$	⋯	$408.41^{+16.53}_{-227.25}$	$132.39^{+156.35}_{-85.59}$	662.39
		Band+BB	$-0.11^{+0.05}_{-0.05}$	$-2.81^{+0.18}_{-0.18}$	$330.91^{+21.43}_{-27.15}$	$243.23^{+18.64}_{-14.67}$	666.15

Table 2
(Continued)

$t_{\rm start}-t_{\rm end}$ (s)	S	Model	α	β	E_p/E_c (keV)	kT (keV)	BIC
(1)	(2)	(3)	(4)	(5)	(6)	(7)	(8)
7.23−8.19	436	CPL	$-0.53^{+0.0}_{-0.0}$	⋯	$711.25^{+6.81}_{-6.87}$	⋯	6451.18
		Band	$-0.48^{+0.01}_{-0.01}$	$-3.33^{+0.07}_{-0.07}$	$957.06^{+10.31}_{-10.9}$	⋯	6294.71
		CPL+BB	$-0.53^{+0.01}_{-0.01}$	⋯	$842.17^{+6.81}_{-11.38}$	$52.56^{+1.26}_{-1.28}$	5564.47
		Band+BB	$-0.52^{+0.01}_{-0.01}$	$-4.26^{+0.14}_{-0.14}$	$1193.85^{+14.38}_{-13.81}$	$50.96^{+1.27}_{-1.24}$	5601.16
8.19−8.87	385	CPL	$-0.5^{+0.01}_{-0.01}$	⋯	$526.51^{+6.3}_{-6.32}$	⋯	4648.5
		Band	$-0.46^{+0.01}_{-0.01}$	$-3.33^{+0.07}_{-0.07}$	$729.68^{+8.51}_{-8.46}$	⋯	4546.85
		CPL+BB	$-0.51^{+0.01}_{-0.01}$	⋯	$623.66^{+6.3}_{-10.5}$	$46.12^{+1.37}_{-1.36}$	4133.76
		Band+BB	$-0.24^{+0.01}_{-0.01}$	$-3.0^{+0.09}_{-0.09}$	$393.46^{+11.34}_{-10.4}$	$308.98^{+8.11}_{-7.98}$	4161.35
8.87−9.05	205	CPL	$-0.48^{+0.01}_{-0.01}$	⋯	$677.01^{+15.36}_{-15.59}$	⋯	1993.75
		Band	$-0.45^{+0.01}_{-0.01}$	$-3.52^{+0.16}_{-0.16}$	$955.68^{+20.99}_{-21.17}$	⋯	2012.78
		CPL+BB	$-0.49^{+0.02}_{-0.02}$	⋯	$780.46^{+15.36}_{-24.62}$	$52.85^{+3.06}_{-3.01}$	1866.2
		Band+BB	$-0.46^{+0.02}_{-0.02}$	$-4.01^{+0.2}_{-0.19}$	$1121.62^{+20.8}_{-21.5}$	$51.1^{+2.58}_{-2.62}$	1925.39
9.05−9.22	218	CPL	$-0.49^{+0.01}_{-0.01}$	⋯	$374.82^{+8.69}_{-8.7}$	⋯	1921.88
		Band	$-0.41^{+0.02}_{-0.02}$	$-2.99^{+0.09}_{-0.09}$	$496.35^{+11.22}_{-11.3}$	⋯	1872.71
		CPL+BB	$-0.2^{+0.02}_{-0.01}$	⋯	$171.42^{+8.69}_{-11.21}$	$257.29^{+8.29}_{-1.84}$	1732.33
		Band+BB	$-0.16^{+0.04}_{-0.04}$	$-2.9^{+0.15}_{-0.16}$	$286.74^{+15.35}_{-15.92}$	$229.84^{+12.87}_{-12.52}$	1755.71
9.22−9.45	239	CPL	$-0.62^{+0.01}_{-0.01}$	⋯	$741.24^{+15.6}_{-15.23}$	⋯	2559.58
		Band	$-0.59^{+0.01}_{-0.01}$	$-3.27^{+0.1}_{-0.1}$	$934.94^{+18.94}_{-18.24}$	⋯	2540.96
		CPL+BB	$-0.61^{+0.01}_{-0.01}$	⋯	$866.7^{+15.6}_{-24.64}$	$43.07^{+1.82}_{-1.8}$	2320.51
		Band+BB	$-0.5^{+0.22}_{-0.1}$	$-3.42^{+0.88}_{-0.48}$	$914.29^{+243.67}_{-551.58}$	$127.21^{+214.12}_{-87.78}$	2354.43
9.45−9.53	134	CPL	$-0.65^{+0.01}_{-0.01}$	⋯	$1455.55^{+59.18}_{-59.31}$	⋯	1171.67
		Band	$-0.57^{+0.02}_{-0.02}$	$-2.56^{+0.08}_{-0.08}$	$1508.56^{+62.19}_{-61.62}$	⋯	1067.4
		CPL+BB	$-0.66^{+0.02}_{-0.02}$	⋯	$1717.77^{+59.18}_{-86.87}$	$63.78^{+5.64}_{-5.56}$	1110.01
		Band+BB	$-0.58^{+0.02}_{-0.02}$	$-2.66^{+0.09}_{-0.09}$	$1737.18^{+77.11}_{-79.64}$	$54.95^{+5.04}_{-5.33}$	1045.9
9.53−9.79	254	CPL	$-0.5^{+0.01}_{-0.01}$	⋯	$504.69^{+9.04}_{-9.31}$	⋯	2527.04
		Band	$-0.48^{+0.01}_{-0.01}$	$-3.65^{+0.14}_{-0.14}$	$719.6^{+11.41}_{-11.03}$	⋯	2544.92
		CPL+BB	$-0.51^{+0.01}_{-0.02}$	⋯	$578.58^{+9.04}_{-14.21}$	$44.71^{+2.0}_{-2.13}$	2377.4
		Band+BB	$-0.24^{+0.03}_{-0.03}$	$-3.11^{+0.17}_{-0.15}$	$360.04^{+13.02}_{-21.6}$	$279.27^{+12.16}_{-7.82}$	2430.49
9.79−10.21	302	CPL	$-0.5^{+0.01}_{-0.01}$	⋯	$648.64^{+9.6}_{-9.46}$	⋯	3501.83
		Band	$-0.48^{+0.01}_{-0.01}$	$-3.82^{+0.15}_{-0.15}$	$934.32^{+12.09}_{-12.07}$	⋯	3524.88
		CPL+BB	$-0.48^{+0.01}_{-0.01}$	⋯	$699.14^{+9.6}_{-13.22}$	$42.67^{+1.95}_{-1.99}$	3317.89
		Band+BB	$-0.47^{+0.01}_{-0.01}$	$-4.16^{+0.17}_{-0.16}$	$1033.87^{+15.55}_{-16.05}$	$42.46^{+1.61}_{-1.58}$	3372.91
10.21−10.43	246	CPL	$-0.59^{+0.01}_{-0.01}$	⋯	$312.03^{+6.53}_{-6.81}$	⋯	2149.72
		Band	$-0.48^{+0.02}_{-0.02}$	$-2.78^{+0.07}_{-0.07}$	$372.86^{+8.94}_{-8.83}$	⋯	2051.11
		CPL+BB	$-0.31^{+0.03}_{-0.03}$	⋯	$150.7^{+6.53}_{-9.62}$	$231.82^{+11.47}_{-11.81}$	1933.99
		Band+BB	$-0.28^{+0.03}_{-0.03}$	$-2.71^{+0.08}_{-0.09}$	$233.13^{+10.5}_{-10.75}$	$177.29^{+9.13}_{-8.61}$	1938.82
10.43−10.75	272	CPL	$-0.57^{+0.01}_{-0.01}$	⋯	$725.24^{+12.81}_{-12.91}$	⋯	2965.09
		Band	$-0.55^{+0.01}_{-0.01}$	$-3.62^{+0.14}_{-0.13}$	$982.17^{+15.0}_{-15.55}$	⋯	2970.34
		CPL+BB	$-0.56^{+0.01}_{-0.01}$	⋯	$795.63^{+12.81}_{-18.06}$	$43.42^{+2.24}_{-2.18}$	2811.07
		Band+BB	$-0.54^{+0.01}_{-0.01}$	$-3.94^{+0.16}_{-0.15}$	$1095.01^{+17.57}_{-17.37}$	$41.37^{+2.18}_{-2.24}$	2850.37
10.75−10.88	198	CPL	$-0.56^{+0.02}_{-0.02}$	⋯	$285.41^{+7.5}_{-7.6}$	⋯	1492.78
		Band	$-0.45^{+0.02}_{-0.02}$	$-2.75^{+0.08}_{-0.08}$	$345.24^{+8.55}_{-9.59}$	⋯	1443.34
		CPL+BB	$-0.29^{+0.02}_{-0.02}$	⋯	$139.59^{+7.5}_{-6.82}$	$206.28^{+7.55}_{-7.87}$	1371.07
		Band+BB	$-0.25^{+0.04}_{-0.04}$	$-2.69^{+0.11}_{-0.11}$	$222.35^{+13.68}_{-14.01}$	$161.36^{+11.27}_{-11.02}$	1379.13
10.88−10.95	132	CPL	$-0.63^{+0.01}_{-0.01}$	⋯	$1067.08^{+38.31}_{-38.27}$	⋯	983.55
		Band	$-0.6^{+0.02}_{-0.02}$	$-3.37^{+0.22}_{-0.22}$	$1335.99^{+52.96}_{-52.33}$	⋯	1012.94
		CPL+BB	$-0.67^{+0.02}_{-0.02}$	⋯	$1299.9^{+38.31}_{-65.56}$	$72.54^{+5.74}_{-5.81}$	928.6
		Band+BB	$-0.66^{+0.02}_{-0.02}$	$-3.82^{+0.26}_{-0.25}$	$1659.12^{+74.84}_{-74.11}$	$71.9^{+5.91}_{-5.89}$	981.74
10.95−11.11	209	CPL	$-0.57^{+0.01}_{-0.01}$	⋯	$376.58^{+9.65}_{-9.85}$	⋯	1735.14
		Band	$-0.44^{+0.03}_{-0.02}$	$-2.57^{+0.09}_{0.04}$	$419.72^{+-2.91}_{-19.79}$	⋯	1673.57
		CPL+BB	$-0.3^{+0.02}_{-0.02}$	⋯	$174.94^{+9.65}_{-7.97}$	$270.21^{+7.75}_{-9.96}$	1576.18
		Band+BB	$-0.29^{+0.03}_{-0.03}$	$-2.67^{+0.1}_{-0.1}$	$286.19^{+14.56}_{-14.6}$	$216.31^{+13.9}_{-13.65}$	1579.65
11.11−11.27	178	CPL	$-0.69^{+0.02}_{-0.02}$	⋯	$233.7^{+7.91}_{-7.77}$	⋯	1595.75
		Band	$-0.44^{+0.03}_{-0.03}$	$-2.38^{+0.04}_{-0.04}$	$214.66^{+6.95}_{-7.02}$	⋯	1411.08
		CPL+BB	$-0.36^{+0.04}_{-0.04}$	⋯	$110.54^{+7.91}_{-7.16}$	$200.58^{+15.1}_{-14.73}$	1398.37
		Band+BB	$-0.32^{+0.04}_{-0.04}$	$-2.41^{+0.06}_{-0.07}$	$171.71^{+9.25}_{-9.47}$	$127.8^{+13.7}_{-13.89}$	1382.37

Table 2
(Continued)

$t_{start} - t_{end}$ (s) (1)	S (2)	Model (3)	α (4)	β (5)	E_p/E_c (keV) (6)	kT (keV) (7)	BIC (8)
11.27−11.37	171	CPL	$-0.8^{+0.01}_{-0.01}$	⋯	$810.27^{+31.24}_{-29.37}$	⋯	1281.93
		Band	$-0.7^{+0.02}_{-0.03}$	$-2.45^{+0.07}_{-0.1}$	$712.11^{+71.09}_{-38.24}$	⋯	1213.3
		CPL+BB	$-0.86^{+0.02}_{-0.02}$	⋯	$1103.97^{+31.24}_{-55.17}$	$45.49^{+2.6}_{-2.72}$	1172.97
		Band+BB	$-0.81^{+0.02}_{-0.02}$	$-2.91^{+0.13}_{-0.13}$	$1049.39^{+48.83}_{-47.88}$	$43.68^{+2.38}_{-2.34}$	1171.22
11.37−11.5	157	CPL	$-0.76^{+0.02}_{-0.02}$	⋯	$258.93^{+10.13}_{-9.87}$	⋯	1326.83
		Band	$-0.52^{+0.04}_{-0.04}$	$-2.41^{+0.06}_{-0.06}$	$226.82^{+9.48}_{-9.51}$	⋯	1234.11
		CPL+BB	$-0.39^{+0.04}_{-0.04}$	⋯	$109.4^{+10.13}_{-7.31}$	$193.45^{+11.46}_{-11.68}$	1175.25
		Band+BB	$-0.37^{+0.05}_{-0.05}$	$-2.58^{+0.12}_{-0.12}$	$170.01^{+9.31}_{-9.47}$	$152.0^{+14.85}_{-14.86}$	1191.89
11.5−11.59	112	CPL	$-0.77^{+0.03}_{-0.03}$	⋯	$185.78^{+8.83}_{-9.11}$	⋯	856.37
		Band	$-0.62^{+0.05}_{-0.05}$	$-2.7^{+0.11}_{-0.11}$	$186.91^{+8.4}_{-8.35}$	⋯	852.44
		CPL+BB	$-0.44^{+0.07}_{-0.07}$	⋯	$87.19^{+8.83}_{-9.73}$	$130.51^{+10.75}_{-11.03}$	806.58
		Band+BB	$-0.47^{+0.06}_{-0.06}$	$-3.0^{+0.24}_{-0.24}$	$140.85^{+10.04}_{-10.3}$	$115.39^{+12.23}_{-12.13}$	835.56
11.59−11.7	98	CPL	$-0.9^{+0.03}_{-0.03}$	⋯	$188.34^{+11.62}_{-11.88}$	⋯	891.61
		Band	$-0.51^{+0.06}_{-0.06}$	$-2.28^{+0.06}_{-0.05}$	$127.51^{+7.42}_{-7.12}$	⋯	846.1
		CPL+BB	$-0.34^{+0.09}_{-0.09}$	⋯	$60.77^{+11.62}_{-7.22}$	$119.03^{+9.95}_{-9.92}$	812.27
		Band+BB	$-0.5^{+0.05}_{-0.05}$	$-2.36^{+0.1}_{-0.09}$	$116.6^{+5.35}_{-4.91}$	$87.0^{+14.75}_{-15.79}$	824.15
11.7−11.85	96	CPL	$-0.9^{+0.04}_{-0.04}$	⋯	$137.13^{+8.32}_{-8.53}$	⋯	1125.27
		Band	$-0.69^{+0.07}_{-0.06}$	$-2.59^{+0.09}_{-0.1}$	$118.35^{+6.04}_{-6.46}$	⋯	1108.26
		CPL+BB	$-0.56^{+0.08}_{-0.07}$	⋯	$67.12^{+8.32}_{-7.69}$	$102.08^{+11.52}_{-11.06}$	1083.13
		Band+BB	$-0.59^{+0.08}_{-0.08}$	$-2.65^{+0.14}_{-0.14}$	$100.85^{+9.57}_{-9.31}$	$67.3^{+14.83}_{-12.17}$	1098.63
11.85−12.01	123	CPL	$-0.81^{+0.03}_{-0.03}$	⋯	$175.39^{+8.0}_{-8.0}$	⋯	1269.39
		Band	$-0.62^{+0.05}_{-0.05}$	$-2.5^{+0.08}_{-0.08}$	$162.76^{+8.24}_{-8.21}$	⋯	1233.68
		CPL+BB	$-0.47^{+0.07}_{-0.07}$	⋯	$81.72^{+8.0}_{-9.61}$	$120.54^{+11.34}_{-11.23}$	1213.53
		Band+BB	$-0.43^{+0.07}_{-0.07}$	$-2.39^{+0.08}_{-0.08}$	$115.61^{+8.72}_{-9.4}$	$75.34^{+7.47}_{-7.04}$	1218.44
12.01−12.09	78	CPL	$-0.89^{+0.05}_{-0.05}$	⋯	$144.47^{+10.78}_{-10.92}$	⋯	567.46
		Band	$-0.74^{+0.07}_{-0.07}$	$-2.79^{+0.15}_{-0.15}$	$134.22^{+8.09}_{-8.07}$	⋯	572.7
		CPL+BB	$-0.59^{+0.08}_{-0.08}$	⋯	$74.77^{+10.78}_{-9.44}$	$109.73^{+12.38}_{-12.14}$	541.45
		Band+BB	$-0.68^{+0.09}_{-0.09}$	$-2.89^{+0.21}_{-0.21}$	$118.02^{+14.64}_{-13.6}$	$71.19^{+26.86}_{-36.87}$	565.71
12.09−12.23	87	CPL	$-0.9^{+0.04}_{-0.04}$	⋯	$125.14^{+8.26}_{-8.2}$	⋯	965.03
		Band	$-0.69^{+0.08}_{-0.08}$	$-2.6^{+0.12}_{-0.13}$	$109.88^{+8.17}_{-7.85}$	⋯	963.4
		CPL+BB	$-0.51^{+0.11}_{-0.1}$	⋯	$57.11^{+8.26}_{-9.31}$	$81.47^{+9.59}_{-9.49}$	943.2
		Band+BB	$-0.57^{+0.09}_{-0.08}$	$-2.61^{+0.12}_{-0.12}$	$89.77^{+7.31}_{-7.44}$	$60.06^{+8.42}_{-7.16}$	952.55
12.23−12.37	78	CPL	$-1.04^{+0.05}_{-0.05}$	⋯	$130.77^{+11.06}_{-11.15}$	⋯	990.26
		Band	$-0.72^{+0.09}_{-0.09}$	$-2.46^{+0.08}_{-0.08}$	$89.68^{+5.87}_{-5.98}$	⋯	968.23
		CPL+BB	$-0.61^{+0.08}_{-0.08}$	⋯	$56.06^{+11.06}_{-5.75}$	$98.58^{+9.21}_{-9.57}$	944.6
		Band+BB	$-0.67^{+0.1}_{-0.1}$	$-2.49^{+0.12}_{-0.11}$	$83.56^{+7.32}_{-7.21}$	$47.85^{+24.67}_{-24.7}$	959.72
12.37−12.49	63	CPL	$-0.99^{+0.05}_{-0.05}$	⋯	$124.05^{+10.09}_{-10.6}$	⋯	864.19
		Band	$-0.78^{+0.11}_{-0.11}$	$-2.54^{+0.16}_{-0.15}$	$98.48^{+9.74}_{-9.74}$	⋯	868.76
		CPL+BB	$-0.6^{+0.14}_{-0.14}$	⋯	$53.52^{+10.09}_{-11.56}$	$69.46^{+8.18}_{-7.69}$	853.02
		Band+BB	$-0.66^{+0.12}_{-0.12}$	$-2.58^{+0.17}_{-0.16}$	$80.07^{+10.84}_{-10.33}$	$52.99^{+9.84}_{-8.39}$	864.15
12.49−12.57	66	CPL	$-0.98^{+0.05}_{-0.05}$	⋯	$215.92^{+20.75}_{-21.0}$	⋯	515.06
		Band	$-0.86^{+0.08}_{-0.08}$	$-2.51^{+0.18}_{-0.17}$	$177.62^{+18.4}_{-18.64}$	⋯	519.88
		CPL+BB	$-0.71^{+0.09}_{-0.08}$	⋯	$94.76^{+20.75}_{-19.08}$	$108.04^{+13.65}_{-7.97}$	497.62
		Band+BB	$-0.73^{+0.13}_{-0.13}$	$-2.51^{+0.19}_{-0.19}$	$130.02^{+31.35}_{-25.45}$	$78.28^{+20.79}_{-26.57}$	510.05
12.57−12.81	128	CPL	$-0.95^{+0.02}_{-0.02}$	⋯	$306.53^{+15.67}_{-15.5}$	⋯	1739.97
		Band	$-0.79^{+0.04}_{-0.04}$	$-2.43^{+0.09}_{-0.08}$	$237.89^{+13.68}_{-13.7}$	⋯	1703.19
		CPL+BB	$-0.63^{+0.03}_{-0.03}$	⋯	$118.58^{+15.67}_{-7.11}$	$187.61^{+8.78}_{-9.82}$	1650.81
		Band+BB	$-0.64^{+0.04}_{-0.04}$	$-2.78^{+0.22}_{-0.23}$	$165.03^{+9.53}_{-9.74}$	$163.83^{+16.59}_{-16.05}$	1669.95
12.81−12.96	145	CPL	$-0.84^{+0.02}_{-0.02}$	⋯	$538.57^{+23.21}_{-23.29}$	⋯	1488.32
		Band	$-0.81^{+0.02}_{-0.02}$	$-2.81^{+0.14}_{-0.13}$	$561.95^{+23.78}_{-23.57}$	⋯	1482.94
		CPL+BB	$-0.89^{+0.02}_{-0.02}$	⋯	$646.19^{+23.21}_{-42.67}$	$39.29^{+3.98}_{-3.95}$	1477.54
		Band+BB	$-0.64^{+0.04}_{-0.03}$	$-2.4^{+0.09}_{-0.08}$	$282.02^{+15.55}_{-28.41}$	$201.21^{+14.61}_{-10.44}$	1454.94
12.96−13.15	129	CPL	$-0.84^{+0.02}_{-0.02}$	⋯	$251.59^{+11.12}_{-11.16}$	⋯	1471.87
		Band	$-0.75^{+0.03}_{-0.03}$	$-2.75^{+0.13}_{-0.13}$	$247.62^{+11.25}_{-10.98}$	⋯	1467.12
		CPL+BB	$-0.57^{+0.05}_{-0.05}$	⋯	$113.15^{+11.12}_{-12.0}$	$156.56^{+13.38}_{-11.9}$	1418.15
		Band+BB	$-0.56^{+0.05}_{-0.05}$	$-2.87^{+0.22}_{-0.22}$	$157.79^{+13.04}_{-13.03}$	$130.45^{+13.02}_{-13.11}$	1437.06

Table 2
(Continued)

$t_{start} - t_{end}$ (s) (1)	S (2)	Model (3)	α (4)	β (5)	E_p/E_c (keV) (6)	kT (keV) (7)	BIC (8)
13.15−13.3	99	CPL	$-0.88^{+0.03}_{-0.03}$	⋯	$172.22^{+10.01}_{-10.22}$	⋯	1089.41
		Band	$-0.77^{+0.05}_{-0.05}$	$-2.69^{+0.15}_{-0.14}$	$163.08^{+9.17}_{-9.45}$	⋯	1084.75
		CPL+BB	$-0.66^{+0.07}_{-0.06}$	⋯	$96.47^{+10.01}_{-12.99}$	$123.08^{+14.71}_{-14.28}$	1064.5
		Band+BB	$-0.71^{+0.09}_{-0.08}$	$-2.6^{+0.14}_{-0.14}$	$140.15^{+23.96}_{-22.6}$	$59.22^{+21.65}_{-31.42}$	1077.4
13.3−13.47	96	CPL	$-0.91^{+0.04}_{-0.04}$	⋯	$129.76^{+7.99}_{-7.74}$	⋯	1235.46
		Band	$-0.63^{+0.08}_{-0.08}$	$-2.5^{+0.09}_{-0.09}$	$105.49^{+6.64}_{-6.65}$	⋯	1217.32
		CPL+BB	$-0.46^{+0.09}_{-0.09}$	⋯	$54.03^{+7.99}_{-6.68}$	$86.5^{+8.32}_{-8.15}$	1191.07
		Band+BB	$-0.48^{+0.08}_{-0.08}$	$-2.56^{+0.12}_{-0.12}$	$84.6^{+5.88}_{-6.18}$	$62.92^{+8.24}_{-7.83}$	1203.82
13.47−13.74	98	CPL	$-1.04^{+0.04}_{-0.04}$	⋯	$136.03^{+8.5}_{-8.29}$	⋯	1620.09
		Band	$-0.73^{+0.08}_{-0.07}$	$-2.44^{+0.08}_{-0.08}$	$93.25^{+6.26}_{-5.99}$	⋯	1592.65
		CPL+BB	$-0.59^{+0.08}_{-0.08}$	⋯	$54.3^{+8.5}_{-6.25}$	$87.06^{+7.36}_{-7.54}$	1564.77
		Band+BB	$-0.62^{+0.08}_{-0.08}$	$-2.61^{+0.14}_{-0.14}$	$78.65^{+5.21}_{-5.1}$	$65.72^{+9.7}_{-9.26}$	1577.49
13.74−14.0	77	CPL	$-1.06^{+0.05}_{-0.05}$	⋯	$111.04^{+9.04}_{-9.09}$	⋯	1475.25
		Band	$-0.88^{+0.06}_{-0.06}$	$-2.6^{+0.09}_{-0.09}$	$84.46^{+3.72}_{-3.85}$	⋯	1459.98
		CPL+BB	$-0.74^{+0.09}_{-0.09}$	⋯	$56.54^{+9.04}_{-7.88}$	$82.81^{+12.86}_{-12.37}$	1446.67
		Band+BB	$-0.76^{+0.1}_{-0.1}$	$-2.52^{+0.1}_{-0.1}$	$74.12^{+6.8}_{-6.68}$	$37.51^{+12.94}_{-14.43}$	1454.52
14.0−14.47	82	CPL	$-1.21^{+0.04}_{-0.04}$	⋯	$111.05^{+8.5}_{-8.86}$	⋯	2052.1
		Band	$-0.97^{+0.08}_{-0.09}$	$-2.61^{+0.1}_{-0.09}$	$69.56^{+4.36}_{-4.37}$	⋯	2040.61
		CPL+BB	$-0.83^{+0.09}_{-0.09}$	⋯	$49.63^{+8.5}_{-6.78}$	$70.17^{+8.15}_{-8.15}$	2016.96
		Band+BB	$-0.87^{+0.1}_{-0.1}$	$-2.74^{+0.19}_{-0.2}$	$60.34^{+5.59}_{-5.39}$	$48.05^{+12.95}_{-11.76}$	2032.02
14.47−15.4	87	CPL	$-1.39^{+0.04}_{-0.04}$	⋯	$130.82^{+10.24}_{-9.88}$	⋯	2995.52
		Band	$-0.99^{+0.1}_{-0.1}$	$-2.38^{+0.06}_{-0.06}$	$53.45^{+3.75}_{-3.75}$	⋯	2958.41
		CPL+BB	$-0.96^{+0.09}_{-0.08}$	⋯	$47.59^{+10.24}_{-6.21}$	$67.69^{+6.98}_{-7.06}$	2945.81
		Band+BB	$-0.94^{+0.11}_{-0.1}$	$-2.41^{+0.07}_{-0.07}$	$49.14^{+3.94}_{-4.02}$	$35.46^{+9.73}_{-9.45}$	2951.62
15.4−15.53	56	CPL	$-1.28^{+0.04}_{-0.04}$	⋯	$344.36^{+49.24}_{-52.15}$	⋯	794.9
		Band	$-1.11^{+0.09}_{-0.1}$	$-2.24^{+0.15}_{-0.14}$	$159.78^{+29.79}_{-29.06}$	⋯	792.02
		CPL+BB	$-0.96^{+0.12}_{-0.1}$	⋯	$111.68^{+49.24}_{-34.81}$	$115.67^{+18.49}_{-8.12}$	776.71
		Band+BB	$-1.06^{+0.13}_{-0.12}$	$-2.27^{+0.18}_{-0.18}$	$132.68^{+36.55}_{-35.09}$	$59.91^{+38.85}_{-37.38}$	784.92
15.53−16.01	125	CPL	$-1.18^{+0.02}_{-0.02}$	⋯	$236.61^{+13.61}_{-13.82}$	⋯	2454.33
		Band	$-0.93^{+0.05}_{-0.05}$	$-2.27^{+0.05}_{-0.05}$	$124.66^{+7.43}_{-7.42}$	⋯	2391.35
		CPL+BB	$-0.81^{+0.05}_{-0.06}$	⋯	$82.01^{+13.61}_{-8.15}$	$125.8^{+9.59}_{-9.35}$	2364.08
		Band+BB	$-0.82^{+0.05}_{-0.05}$	$-2.49^{+0.13}_{-0.12}$	$98.35^{+5.5}_{-5.55}$	$99.96^{+11.71}_{-11.29}$	2366.82
16.01−16.52	117	CPL	$-1.17^{+0.03}_{-0.03}$	⋯	$184.96^{+11.18}_{-10.79}$	⋯	2475.03
		Band	$-0.92^{+0.06}_{-0.06}$	$-2.33^{+0.06}_{-0.06}$	$104.46^{+6.67}_{-6.61}$	⋯	2410.21
		CPL+BB	$-0.86^{+0.05}_{-0.05}$	⋯	$79.87^{+11.18}_{-7.5}$	$123.62^{+9.51}_{-9.77}$	2391.26
		Band+BB	$-0.62^{+0.09}_{-0.09}$	$-2.19^{+0.05}_{-0.05}$	$65.49^{+6.22}_{-6.8}$	$45.01^{+4.66}_{-4.69}$	2401.67
16.52−16.83	81	CPL	$-1.24^{+0.04}_{-0.04}$	⋯	$176.99^{+16.07}_{-16.36}$	⋯	1681.77
		Band	$-0.98^{+0.09}_{-0.09}$	$-2.31^{+0.08}_{-0.08}$	$91.34^{+9.1}_{-8.75}$	⋯	1657.52
		CPL+BB	$-0.92^{+0.09}_{-0.09}$	⋯	$73.27^{+16.07}_{-13.51}$	$99.2^{+18.43}_{-17.57}$	1654.47
		Band+BB	$-0.82^{+0.14}_{-0.14}$	$-2.26^{+0.08}_{-0.08}$	$69.77^{+12.5}_{-11.19}$	$45.83^{+8.54}_{-7.01}$	1655.2
16.83−17.25	106	CPL	$-1.18^{+0.03}_{-0.03}$	⋯	$216.24^{+13.84}_{-14.44}$	⋯	2225.51
		Band	$-0.93^{+0.06}_{-0.07}$	$-2.28^{+0.07}_{-0.07}$	$116.3^{+9.96}_{-9.59}$	⋯	2196.09
		CPL+BB	$-0.79^{+0.07}_{-0.07}$	⋯	$72.27^{+13.84}_{-9.28}$	$107.06^{+9.88}_{-9.63}$	2164.34
		Band+BB	$-0.68^{+0.08}_{-0.08}$	$-2.29^{+0.1}_{-0.09}$	$75.58^{+6.38}_{-6.26}$	$67.09^{+8.91}_{-9.37}$	2170.57
17.25−17.85	145	CPL	$-1.14^{+0.02}_{-0.02}$	⋯	$331.5^{+16.94}_{-16.2}$	⋯	2858.74
		Band	$-1.03^{+0.03}_{-0.03}$	$-2.32^{+0.07}_{-0.06}$	$210.69^{+11.92}_{-12.71}$	⋯	2815.95
		CPL+BB	$-0.86^{+0.03}_{-0.03}$	⋯	$115.37^{+16.94}_{-7.35}$	$149.75^{+7.48}_{-7.12}$	2789.97
		Band+BB	$-0.73^{+0.07}_{-0.07}$	$-2.16^{+0.06}_{-0.06}$	$102.75^{+9.4}_{-10.15}$	$87.21^{+7.41}_{-7.49}$	2777.81
17.85−18.07	74	CPL	$-1.23^{+0.03}_{-0.03}$	⋯	$309.83^{+30.84}_{-30.87}$	⋯	1363.22
		Band	$-1.15^{+0.06}_{-0.06}$	$-2.38^{+0.17}_{-0.16}$	$188.39^{+22.02}_{-22.57}$	⋯	1361.44
		CPL+BB	$-1.03^{+0.11}_{-0.18}$	⋯	$149.82^{+30.84}_{-59.72}$	$96.26^{+26.74}_{-64.77}$	1346.48
		Band+BB	$-0.94^{+0.14}_{-0.14}$	$-2.19^{+0.13}_{-0.13}$	$104.43^{+23.81}_{-26.66}$	$67.25^{+15.11}_{-10.22}$	1349.45
18.07−18.3	65	CPL	$-1.33^{+0.04}_{-0.04}$	⋯	$287.94^{+37.18}_{-36.01}$	⋯	1328.58
		Band	$-0.95^{+0.12}_{-0.12}$	$-2.1^{+0.06}_{-0.06}$	$92.72^{+12.57}_{-13.07}$	⋯	1314.38
		CPL+BB	$-0.83^{+0.11}_{-0.11}$	⋯	$61.71^{+37.18}_{-11.57}$	$97.39^{+10.54}_{-9.45}$	1298.3
		Band+BB	$-0.85^{+0.11}_{-0.1}$	$-2.24^{+0.13}_{-0.13}$	$73.72^{+6.74}_{-7.6}$	$71.63^{+13.22}_{-11.1}$	1299.59

Table 2
(Continued)

$t_{start} - t_{end}$ (s) (1)	S (2)	Model (3)	α (4)	β (5)	E_p/E_c (keV) (6)	kT (keV) (7)	BIC (8)
18.3−18.61	63	CPL	$-1.34^{+0.05}_{-0.05}$	⋯	$194.63^{+24.47}_{-24.06}$	⋯	1549.76
		Band	$-1.09^{+0.1}_{-0.1}$	$-2.35^{+0.1}_{-0.1}$	$87.42^{+9.16}_{-9.0}$	⋯	1540.69
		CPL+BB	$-0.95^{+0.09}_{-0.09}$	⋯	$65.77^{+24.47}_{-9.94}$	$93.54^{+10.24}_{-10.32}$	1521.62
		Band+BB	$-1.05^{+0.1}_{-0.1}$	$-2.5^{+0.21}_{-0.26}$	$78.74^{+11.11}_{-10.21}$	$51.46^{+30.45}_{-30.28}$	1533.53
18.61−19.27	71	CPL	$-1.48^{+0.04}_{-0.04}$	⋯	$204.9^{+22.64}_{-23.76}$	⋯	2459.59
		Band	$-1.21^{+0.13}_{-0.13}$	$-2.3^{+0.1}_{-0.1}$	$69.37^{+11.35}_{-10.84}$	⋯	2456.44
		CPL+BB	$-1.07^{+0.1}_{-0.1}$	⋯	$55.94^{+22.64}_{-9.89}$	$70.61^{+7.19}_{-6.88}$	2431.91
		Band+BB	$-1.06^{+0.11}_{-0.12}$	$-2.5^{+0.2}_{-0.2}$	$51.54^{+5.49}_{-5.52}$	$54.64^{+9.84}_{-9.14}$	2440.58
19.27−20.46	70	CPL	$-1.61^{+0.04}_{-0.04}$	⋯	$261.02^{+35.28}_{-35.9}$	⋯	3260.69
		Band	$-1.04^{+0.14}_{-0.14}$	$-2.14^{+0.04}_{-0.03}$	$44.76^{+4.42}_{-4.59}$	⋯	3231.85
		CPL+BB	$-1.16^{+0.1}_{-0.1}$	⋯	$55.84^{+35.28}_{-10.26}$	$74.26^{+8.43}_{-8.48}$	3223.3
		Band+BB	$-0.99^{+0.13}_{-0.13}$	$-2.19^{+0.06}_{-0.06}$	$41.06^{+3.81}_{-3.83}$	$37.45^{+11.07}_{-11.14}$	3220.55
20.46−21.43	54	CPL	$-1.74^{+0.05}_{-0.05}$	⋯	$270.92^{+54.81}_{-53.88}$	⋯	2928.8
		Band	$-0.95^{+0.16}_{-0.15}$	$-2.19^{+0.04}_{-0.04}$	$32.08^{+2.75}_{-2.74}$	⋯	2904.34
		CPL+BB	$-1.07^{+0.15}_{-0.15}$	⋯	$36.27^{+54.81}_{-7.58}$	$58.13^{+6.45}_{-6.27}$	2891.5
		Band+BB	$-0.98^{+0.13}_{-0.13}$	$-2.28^{+0.1}_{-0.11}$	$31.62^{+2.3}_{-2.33}$	$37.33^{+14.17}_{-15.76}$	2892.02
21.43−22.26	43	CPL	$-1.75^{+0.06}_{-0.06}$	⋯	$225.86^{+54.7}_{-51.77}$	⋯	2642.93
		Band	$-1.25^{+0.16}_{-0.16}$	$-2.31^{+0.07}_{-0.07}$	$35.93^{+4.16}_{-4.22}$	⋯	2640.19
		CPL+BB	$-1.26^{+0.16}_{-0.16}$	⋯	$47.72^{+54.7}_{-13.96}$	$55.29^{+7.13}_{-6.29}$	2622.24
		Band+BB	$-1.21^{+0.16}_{-0.16}$	$-2.54^{+0.22}_{-0.21}$	$32.58^{+3.01}_{-3.07}$	$41.14^{+11.02}_{-12.86}$	2630.09
22.26−23.26	40	CPL	$-1.85^{+0.05}_{-0.05}$	⋯	$585.85^{+188.08}_{-211.75}$	⋯	2847.76
		Band	$-1.29^{+0.18}_{-0.16}$	$-2.09^{+0.04}_{-0.04}$	$29.63^{+5.11}_{-4.91}$	⋯	2848.97
		CPL+BB	$-1.85^{+0.05}_{-0.06}$	⋯	$572.23^{+188.08}_{-220.6}$	$24.11^{+10.77}_{-12.05}$	2836.2
		Band+BB	$-1.3^{+0.14}_{-0.14}$	$-2.16^{+0.08}_{-0.07}$	$27.13^{+4.1}_{-4.02}$	$32.83^{+9.14}_{-8.8}$	2838.47
23.26−25.51	41	CPL	$-1.79^{+0.05}_{-0.05}$	⋯	$460.61^{+135.15}_{-134.84}$	⋯	4101.87
		Band	$-1.27^{+0.19}_{-0.18}$	$-2.08^{+0.05}_{-0.05}$	$34.3^{+7.24}_{-7.2}$	⋯	4099.65
		CPL+BB	$-1.8^{+0.05}_{-0.05}$	⋯	$473.16^{+135.15}_{-145.13}$	$19.18^{+8.14}_{-8.71}$	4095.13
		Band+BB	$-1.21^{+0.22}_{-0.2}$	$-2.12^{+0.06}_{-0.06}$	$29.24^{+5.06}_{-5.2}$	$29.2^{+7.25}_{-7.37}$	4090.94
25.51−29.75	74	CPL	$-2.0^{+0.03}_{-0.03}$	⋯	$336.62^{+60.73}_{-64.98}$	⋯	5232.8
		Band	$-1.13^{+0.16}_{-0.17}$	$-2.31^{+0.02}_{-0.02}$	$21.11^{+0.98}_{-1.01}$	⋯	5175.22
		CPL+BB	$-1.55^{+0.07}_{-0.07}$	⋯	$51.83^{+60.73}_{-6.92}$	$71.84^{+7.04}_{-6.83}$	5163.48
		Band+BB	$-1.12^{+0.16}_{-0.16}$	$-2.31^{+0.03}_{-0.02}$	$20.83^{+1.07}_{-1.04}$	$17.84^{+6.61}_{-7.07}$	5169.04
29.75−30.84	38	CPL	$-2.16^{+0.04}_{-0.04}$	⋯	$1462.28^{+727.64}_{-790.15}$	⋯	2989.92
		Band	$-1.28^{+0.13}_{-0.14}$	$-2.27^{+0.03}_{-0.04}$	$14.81^{+1.48}_{-1.53}$	⋯	2975.44
		CPL+BB	$-1.81^{+0.27}_{-0.34}$	⋯	$276.95^{+727.64}_{-247.63}$	$43.08^{+9.81}_{-6.63}$	2964.5
		Band+BB	$-1.22^{+0.13}_{-0.15}$	$-2.42^{+0.11}_{-0.11}$	$15.03^{+1.28}_{-1.33}$	$39.87^{+8.5}_{-8.07}$	2964.48
30.84−33.13	40	CPL	$-2.16^{+0.03}_{-0.03}$	⋯	$2519.66^{+1204.23}_{-1271.69}$	⋯	4223.53
		Band	$-1.33^{+0.08}_{-0.12}$	$-2.2^{+0.02}_{-0.02}$	$10.99^{+1.48}_{-1.5}$	⋯	4211.95
		CPL+BB	$-2.23^{+0.05}_{-0.06}$	⋯	$1269.2^{+1204.23}_{-919.53}$	$45.54^{+10.28}_{-8.61}$	4198.27
		Band+BB	$-1.23^{+0.16}_{-0.16}$	$-2.32^{+0.07}_{-0.07}$	$11.38^{+1.17}_{-1.13}$	$37.95^{+6.33}_{-5.4}$	4198.4
33.13−37.12	32	CPL	$-1.94^{+0.04}_{-0.04}$	⋯	$1049.3^{+351.52}_{-452.77}$	⋯	4962.03
		Band	$-1.23^{+0.22}_{-0.21}$	$-2.05^{+0.03}_{-0.02}$	$17.65^{+2.34}_{-2.58}$	⋯	4961.85
		CPL+BB	$-1.96^{+0.05}_{-0.04}$	⋯	$1000.42^{+351.52}_{-551.41}$	$20.12^{+7.8}_{-10.08}$	4949.27
		Band+BB	$-1.35^{+0.09}_{-0.09}$	$-2.1^{+0.05}_{-0.05}$	$17.24^{+2.38}_{-2.42}$	$25.46^{+8.24}_{-8.67}$	4951.88
37.12−42.44	22	CPL	$-1.75^{+0.06}_{-0.06}$	⋯	$604.02^{+231.72}_{-251.4}$	⋯	5322.14
		Band	$-1.01^{+0.29}_{-0.3}$	$-1.98^{+0.04}_{-0.04}$	$28.68^{+5.71}_{-6.0}$	⋯	5322.16
		CPL+BB	$-1.73^{+0.09}_{-0.1}$	⋯	$541.91^{+231.72}_{-419.74}$	$25.38^{+22.24}_{-14.58}$	5306.48
		Band+BB	$-0.99^{+0.27}_{-0.27}$	$-2.11^{+0.13}_{-0.13}$	$25.66^{+3.93}_{-4.06}$	$34.41^{+8.65}_{-9.25}$	5311.08
42.44−46.32	16	CPL	$-1.78^{+0.07}_{-0.07}$	⋯	$824.01^{+382.98}_{-430.31}$	⋯	4848.15
		Band	$-1.02^{+0.3}_{-0.3}$	$-1.99^{+0.06}_{-0.06}$	$30.82^{+6.61}_{-6.52}$	⋯	4845.11
		CPL+BB	$-1.78^{+0.07}_{-0.08}$	⋯	$821.91^{+382.98}_{-448.64}$	$16.78^{+7.09}_{-7.49}$	4842.02
		Band+BB	$-0.99^{+0.25}_{-0.27}$	$-2.0^{+0.06}_{-0.06}$	$28.4^{+5.04}_{-5.33}$	$18.25^{+6.59}_{-6.88}$	4837.15
46.32−50.0	10	CPL	$-1.42^{+0.14}_{-0.13}$	⋯	$223.04^{+77.5}_{-84.22}$	⋯	4678.23
		Band	$-1.21^{+0.19}_{-0.2}$	$-2.45^{+0.34}_{-0.33}$	$89.54^{+25.85}_{-29.64}$	⋯	4690.74
		CPL+BB	$-1.47^{+0.2}_{-0.2}$	⋯	$189.87^{+77.5}_{-128.06}$	$30.07^{+10.19}_{-12.56}$	4668.41
		Band+BB	$-0.83^{+0.26}_{-0.28}$	$-2.39^{+0.27}_{-0.26}$	$33.64^{+5.94}_{-8.15}$	$33.69^{+4.59}_{-4.02}$	4674.29

Table 2
(Continued)

$t_{start} - t_{end}$ (s) (1)	S (2)	Model (3)	α (4)	β (5)	E_p/E_c (keV) (6)	kT (keV) (7)	BIC (8)
120.0−121.01	9	CPL	$-1.21^{+0.17}_{-0.2}$	⋯	$168.47^{+85.74}_{-74.65}$	⋯	3556.17
		Band	$-0.67^{+0.24}_{-0.25}$	$-2.16^{+0.18}_{-0.18}$	$57.32^{+15.89}_{-13.65}$	⋯	3562.9
		CPL+BB	$-1.27^{+0.23}_{-0.22}$	⋯	$169.64^{+85.74}_{-97.65}$	$28.05^{+12.82}_{-12.77}$	3547.83
		Band+BB	$-0.6^{+0.25}_{-0.29}$	$-2.12^{+0.14}_{-0.13}$	$44.48^{+10.1}_{-11.34}$	$27.73^{+7.54}_{-8.81}$	3553.92
121.01−122.73	17	CPL	$-1.38^{+0.09}_{-0.09}$	⋯	$287.1^{+70.08}_{-79.95}$	⋯	4463.75
		Band	$-1.31^{+0.1}_{-0.1}$	$-2.51^{+0.32}_{-0.3}$	$144.79^{+32.65}_{-30.64}$	⋯	4471.66
		CPL+BB	$-1.43^{+0.1}_{-0.08}$	⋯	$310.76^{+70.08}_{-94.04}$	$28.59^{+9.66}_{-10.1}$	4455.77
		Band+BB	$-1.0^{+0.17}_{-0.16}$	$-2.23^{+0.21}_{-0.21}$	$56.89^{+10.75}_{-13.76}$	$44.39^{+10.12}_{-9.69}$	4460.24
122.73−125.21	25	CPL	$-1.41^{+0.06}_{-0.06}$	⋯	$362.31^{+84.69}_{-82.59}$	⋯	5133.65
		Band	$-1.22^{+0.13}_{-0.14}$	$-2.22^{+0.21}_{-0.21}$	$131.14^{+37.61}_{-40.45}$	⋯	5133.6
		CPL+BB	$-1.4^{+0.05}_{-0.09}$	⋯	$376.29^{+84.69}_{-92.53}$	$23.78^{+6.57}_{-11.53}$	5126.67
		Band+BB	$-1.14^{+0.26}_{-0.24}$	$-2.16^{+0.19}_{-0.2}$	$110.47^{+58.76}_{-54.23}$	$28.91^{+16.34}_{-14.28}$	5125.04
125.21−129.71	32	CPL	$-1.35^{+0.05}_{-0.05}$	⋯	$278.28^{+37.87}_{-39.01}$	⋯	5952.97
		Band	$-1.31^{+0.06}_{-0.06}$	$-2.67^{+0.24}_{-0.25}$	$158.28^{+16.16}_{-16.04}$	⋯	5958.68
		CPL+BB	$-1.37^{+0.05}_{-0.05}$	⋯	$296.08^{+37.87}_{-46.05}$	$20.76^{+7.93}_{-8.41}$	5945.06
		Band+BB	$-1.2^{+0.22}_{-0.16}$	$-2.52^{+0.28}_{-0.28}$	$125.03^{+46.58}_{-63.8}$	$33.54^{+21.61}_{-19.75}$	5945.96
129.71−142.33	27	CPL	$-1.42^{+0.05}_{-0.05}$	⋯	$218.93^{+28.32}_{-28.54}$	⋯	7240.04
		Band	$-1.21^{+0.1}_{-0.1}$	$-2.43^{+0.12}_{-0.12}$	$91.72^{+11.56}_{-11.88}$	⋯	7229.33
		CPL+BB	$-1.45^{+0.06}_{-0.06}$	⋯	$241.32^{+28.32}_{-41.69}$	$20.21^{+6.62}_{-7.17}$	7231.79
		Band+BB	$-1.05^{+0.27}_{-0.23}$	$-2.31^{+0.14}_{-0.14}$	$70.5^{+25.54}_{-24.53}$	$29.35^{+9.1}_{-12.37}$	7224.8
142.33−148.82	20	CPL	$-1.4^{+0.07}_{-0.07}$	⋯	$145.52^{+21.87}_{-22.44}$	⋯	5735.9
		Band	$-1.0^{+0.24}_{-0.24}$	$-2.46^{+0.14}_{-0.14}$	$57.0^{+11.33}_{-10.97}$	⋯	5736.26
		CPL+BB	$-1.05^{+0.25}_{-0.33}$	⋯	$70.02^{+21.87}_{-34.01}$	$47.12^{+14.67}_{-26.12}$	5723.35
		Band+BB	$-0.82^{+0.23}_{-0.24}$	$-2.45^{+0.12}_{-0.12}$	$45.12^{+7.11}_{-7.26}$	$33.66^{+8.48}_{-8.25}$	5727.17
148.82−154.1	18	CPL	$-1.21^{+0.09}_{-0.09}$	⋯	$82.27^{+11.96}_{-11.81}$	⋯	5062.25
		Band	$-1.03^{+0.15}_{-0.16}$	$-2.95^{+0.23}_{-0.23}$	$55.11^{+5.63}_{-5.72}$	⋯	5074.45
		CPL+BB	$-1.09^{+0.22}_{-0.19}$	⋯	$63.47^{+11.96}_{-26.27}$	$31.94^{+13.05}_{-16.59}$	5055.4
		Band+BB	$-0.94^{+0.2}_{-0.19}$	$-2.91^{+0.21}_{-0.21}$	$47.4^{+8.25}_{-7.91}$	$29.03^{+7.96}_{-9.35}$	5068.38
154.1−162.66	16	CPL	$-1.04^{+0.13}_{-0.14}$	⋯	$56.38^{+8.87}_{-8.77}$	⋯	5163.54
		Band	$-0.93^{+0.17}_{-0.17}$	$-3.36^{+0.25}_{-0.25}$	$49.24^{+3.65}_{-3.42}$	⋯	5188.43
		CPL+BB	$-1.03^{+0.14}_{-0.15}$	⋯	$52.55^{+8.87}_{-9.97}$	$23.72^{+8.87}_{-9.62}$	5155.1
		Band+BB	$-0.91^{+0.18}_{-0.17}$	$-3.32^{+0.23}_{-0.23}$	$45.58^{+5.08}_{-5.07}$	$23.35^{+6.76}_{-8.03}$	5179.71
162.66−170.0	14	CPL	$-0.71^{+0.13}_{-0.12}$	⋯	$39.93^{+4.82}_{-4.87}$	⋯	4745.95
		Band	$-0.61^{+0.16}_{-0.17}$	$-3.58^{+0.24}_{-0.24}$	$47.78^{+3.0}_{-3.04}$	⋯	4781.97
		CPL+BB	$-0.68^{+0.14}_{-0.14}$	⋯	$37.87^{+4.82}_{-5.17}$	$21.36^{+7.36}_{-8.03}$	4738.12
		Band+BB	$-0.59^{+0.18}_{-0.17}$	$-3.59^{+0.24}_{-0.24}$	$45.96^{+3.26}_{-3.3}$	$21.51^{+6.05}_{-6.54}$	4770.41

Yu et al. (2018) found a "tracking" trend for E_p. In Figure 3 we show the evolution of the parameter α over time for the two GRBs. For GRB 160509A, the α in the main burst does not have either of the above evolutionary trends over time as seen in Figure 3, where α in five time-resolved spectra exceed the synchrotron dead line, and the number of α exceeding the synchrotron dead line increases to 7 with the addition of the BB component. For the postburst (Figure 3), α has no obvious evolution trend, and the number of α that exceeds the synchrotron dead line is 4. The evolution of α over time does not change significantly with the addition of the BB, but the number of α that exceeds the synchrotron dead line is 8. For GRB 130427A, the evolution of α over time in the main burst (Figure 3) shows hard-to-soft and then tracking behavior, and there are 42 time-resolved spectra that exceed the synchrotron dead line. The evolution mode of α over time does not change with the addition of the BB component and the number of $\alpha > -2/3$ increases to 54. In the postburst (Figure 3), α appears to be a soft-to-hard evolution trend, and none of α exceeds the synchrotron dead line.

Figure 4 shows the evolution of E_p over time for GRB 160509A and GRB 130427A. For GRB 160509A, there is a hard-to-soft evolutionary trend of E_p for both the main burst and the postburst. For GRB 130427A, E_p first evolves in a hard-to-soft and then tracks the flux, and has little effect after adding BB for the main burst. In the postburst, there is a hard-to-soft evolution trend in E_p over time and there is no obvious change after adding BB. As shown in Figure 5, the evolution mode of the kT for both the two GRBs shows a same tracking tendency over time for both the main burst and postburst.

4.3. Correlations of Spectral Parameters

Previous studies revealed that there are some correlations among spectral parameters and that correlation analysis plays a

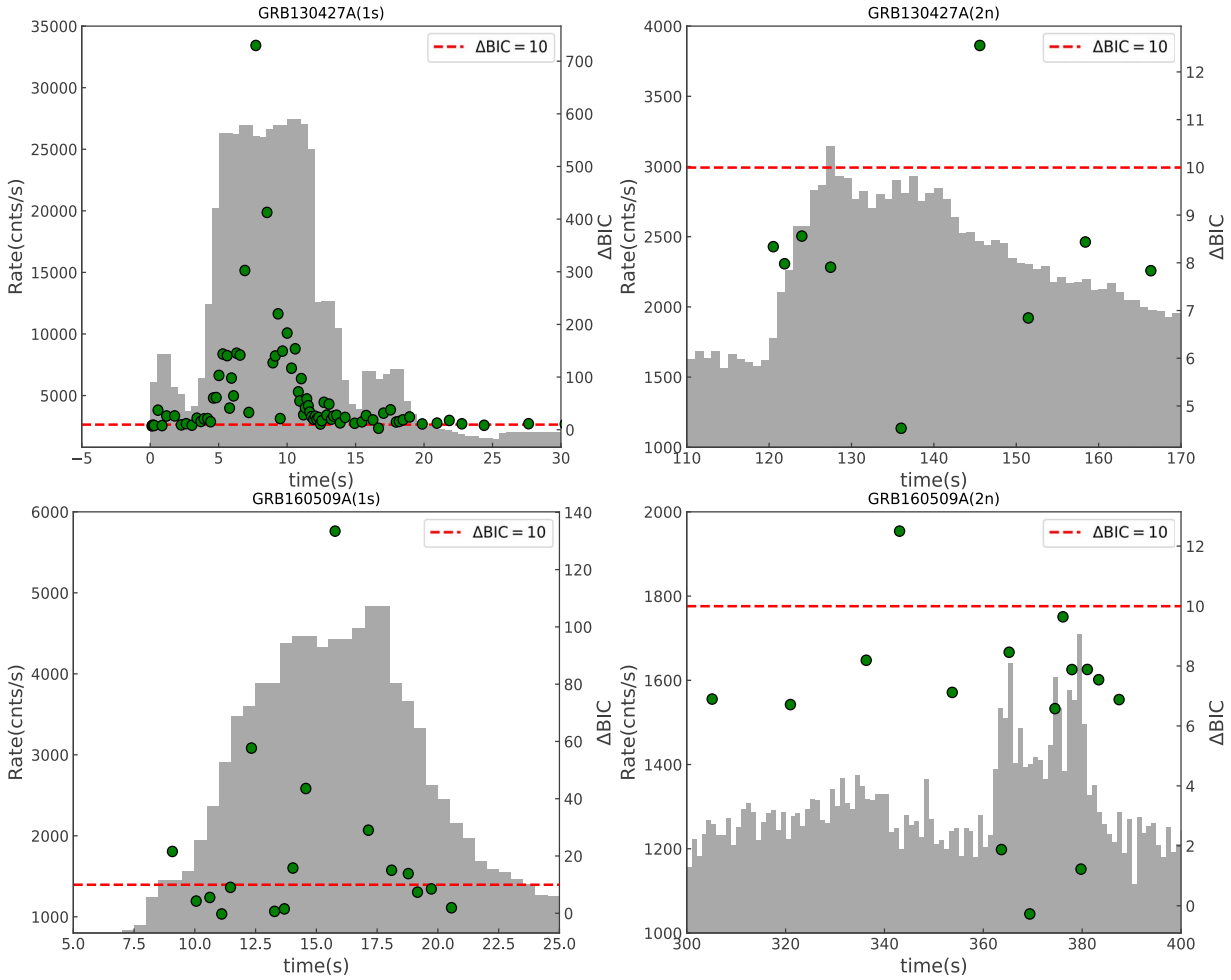

Figure 2. The evolution of ΔBIC over time. The gray shading is the light curve, and the red dotted line indicates ΔBIC = 10.

crucial role in understanding the physical processes of GRBs, which provides clues to reveal the nature of GRBs. In this section, we systematically investigate and compare the correlations between the main and postburst spectral parameters of GRB 160509A and GRB 130427A in order to provide clues whether the main bursts and postbursts are of the same origin.

Figure 6 shows there is no correlation between α and E_p in the main burst in GRB 160509A ($r=-0.02$, $p=0.93$), but after the addition of BB there is a moderate negative correlations ($r=-0.55$, $p=0.02$). There is no significant correlation ($r=0.03$, $p=0.91$) in the postburst and a weak negative correlation after the addition of BB ($r=-0.34$, $p=0.22$). For the case of GRB 130427A, there is a strong positive correlation ($r=0.74$, $p=3.4\times10^{-15}$) in the main burst and the correlation weakened after the addition of BB ($r=0.48$, $p=1.3\times10^{-6}$). However, the postburst shows a different correlation from the main burst; there is a strong moderate negative correlation in the postburst ($r=-0.62$, $p=0.07$), in addition to an enhanced negative correlation with the addition of BB ($r=-0.93$, $p=2.3\times10^{-4}$).

Figure 7 shows the correlation between α and F. In GRB 160509A the correlation is insignificant ($r=-0.12$, $p=0.64$) for the main burst. For the postburst there is a weak negative correlation ($r=-0.41$, $\mathrm{p}=0.13$). For the case of GRB 130427A, there is a strong positive correlation ($r=0.77$, $p=3.7\times10^{-17}$) for the main burst and the correlation weakens with the addition of BB ($r=0.52$, $p=1.1\times10^{-7}$) and the postburst of $\alpha-\mathrm{F}$ has a same weak negative correlation ($r=-0.4$, $p=0.28$) for both with BB and without BB.

Figure 8 shows the correlation between E_p and F. For GRB 160509A, a weak correlation is obtained for the main burst and the postburst. For the case of GRB 130427A, the main burst yields a strong positive correlation between E_p and F ($r=0.91$, $p=6.8\times10^{-32}$), which is unchanged by the addition of BB. While the correlation ($r=0.18$, $p=0.63$) is very weak for the postburst with BB and without BB.

The above analysis results of GRB 160509A share almost the same correlations for the main and postburst, which seems to indicate that the main bursts and postbursts may have come from the same origin, while for GRB 130427A this conclusion does not seem to be supported.

4.4. Comparison of Amati Relation and Yonetoku Relation between Main Bursts and Postbursts

To further compare the spectral properties of the main bursts and postbursts, we also check whether the main bursts and postbursts follow the same Amati relation and Yonetoku relation (E_p-L_{iso}). In Figure 9, we present the Amati and Yonetoku relation of the time-integrated spectra of GRB 160509A and GRB 130427A. For the Amati relation, it can be seen from the figure that the main burst and the postburst of the

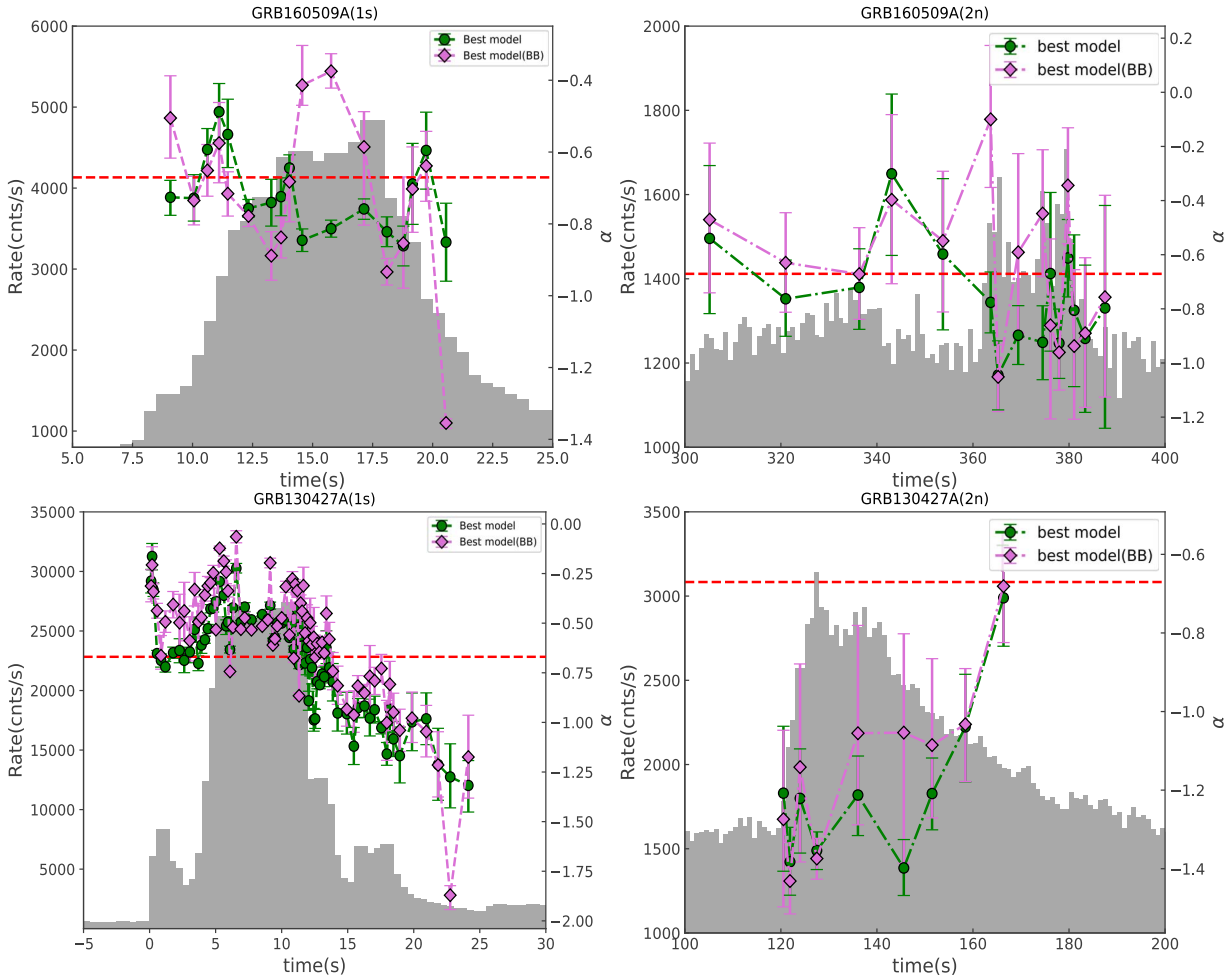

Figure 3. Evolution of the spectral parameter α over time fitted with the best model for the two GRBs, where the green and purple data points represent best model and best model + BB. Top left and right panels are the main bursts and postbursts in GRB 160509A, while bottom left and right panels are the main bursts and postbursts in GRB 130427A. The red dashed line indicates $\alpha = -0.67$.

two bursts conform to the Amati relation. The main and postburst of GRB 130427A deviate from the Amati relation after the addition of the BB component. For the Yonetoku relation, it can be seen from the figure that the main and postburst of the two bursts also conform to the Yonetoku relation. However, the main burst of GRB 160509A with the addition of BB components deviates from the Yonetoku relation, and the postburst is consistent with the addition of BB components and without BB components. Both the main burst and postburst of GRB 130427A deviate from the Yonetoku relation after the addition of the BB component.

The fact that the main bursts and postbursts of both of GRB 160509A and GRB 130427A follow the same Amati relations and Yonetoku relations seems to support the main burst and postburst with the same origin. Therefore, we tend to believe the origin of the main burst and postburst is the same based on the two correlations.

5. Photosphere Radiation Parameters

There are generally two main acceleration mechanisms for a GRB jet: thermally driven and magnetically driven. The thermally driven jet is associated with hot fireballs and develops rapidly, while the magnetically driven jet is associated with Poynting-flux-dominated outflows and is progressing relatively slowly Gao & Zhang (2015). In this section, we would like to examine the radiation sources of the main bursts and postbursts photospheres by constraining the outflow properties of the thermal pulse by some empirical relations.

In early stages of the fireball, it consisted of thermal photons and electron–positron pairs (Goodman 1986; Paczynski & Xu 1994). At some radius above the fireball, a fraction of the outflow kinetic energy is dissipated by some unspecified mechanism, which accelerates the electrons to higher energies. The possible electron distribution in the diffusion shock is a Maxwell–Boltzmann distribution with an extended power law at high energies (Ellison et al. 1995; Spitkovsky 2008). In fact, this electron distribution is consistent with the observations (Tavani 1996; Burgess & Ryde 2015). For each time period, we estimate the outflow parameters $\Re$, Γ, r_0, r_s, $r_{\rm ph}$, blackbody temperature T, using the method described by Pe'Er et al. (2007).

5.1. Parameter $\Re$

Under spherical symmetry (Pe'Er et al. 2007), the ratio of the observed quantities $F_{\rm BB}$ and T is expressed as $\Re$, which can be measured by the following equation (for $r_{\rm ph} > r_s$):

$$\Re = \left(\frac{F_{\rm BB}^{\rm ob}}{\sigma T^{\rm ob^4}}\right)^{1/2} = (1.06)\frac{(1+z)^2}{d_L}\frac{r_{\rm ph}}{\Gamma}, \quad (5)$$

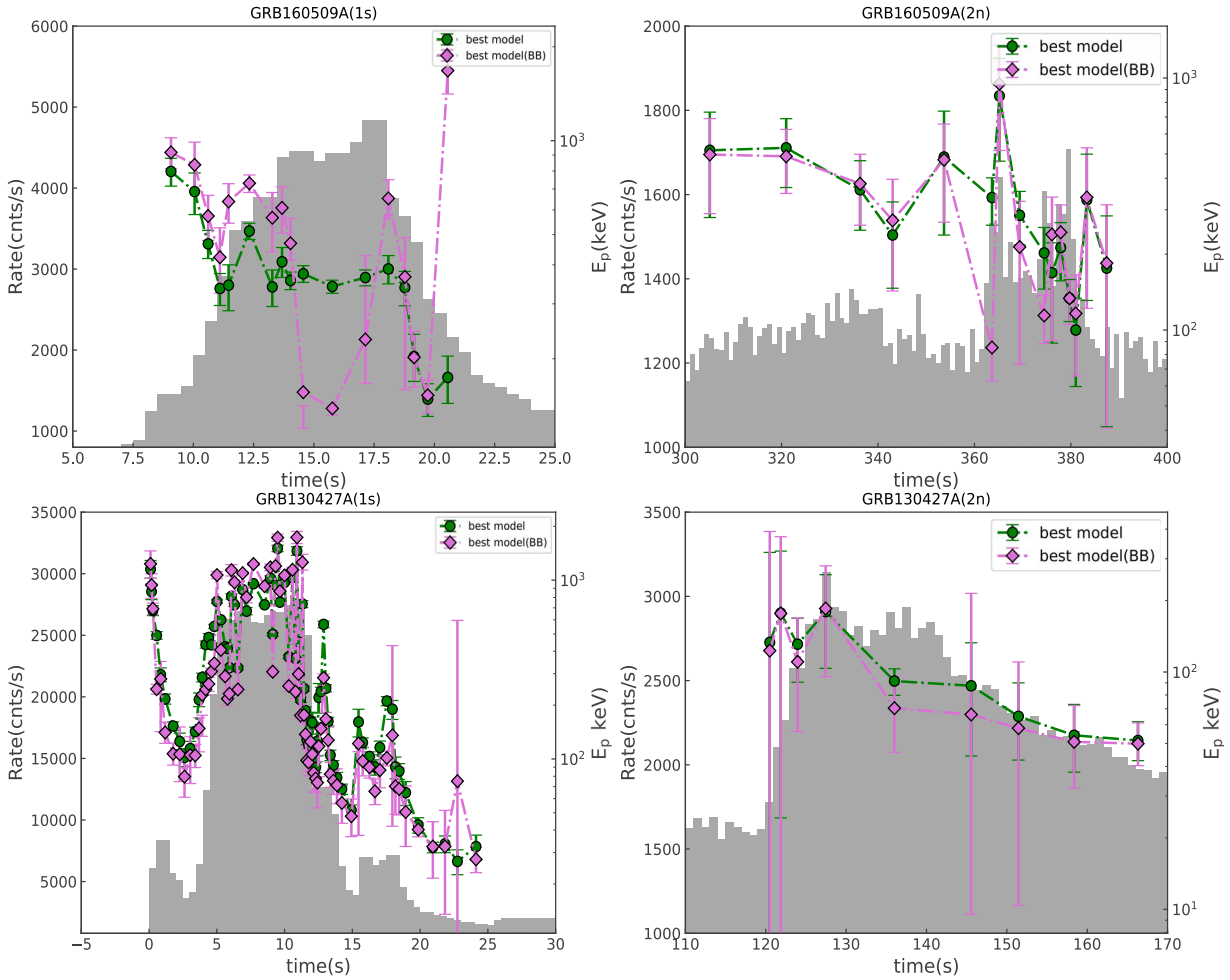

Figure 4. Evolution of the spectral parameter E_p over time fitted with the best model for the two GRBs. All symbols are the same as in Figure 3.

where σ is the Stefan–Boltzmann constant, z is the redshift, and d_L is the photometric distance. For bursts with known redshift, the parameter $\Re$ can be interpreted as the effective lateral size of the radiating area (Ryde & Pe'er 2009). Thus, the constant $\Re$ indicates that the effective radiative area of the photosphere is independent of time.

The time evolution of the parameters $\Re$ for GRB 160509A and GRB 130427A are given in Figure 10, in which it can be seen that the $\Re$ of the main burst of GRB 160509A increases first and then decreases over time. The $\Re$ of the postburst seems to extend the main burst. The mean values of the main bursts and postbursts $\Re$ are $10^{-18.31\pm0.32}$ and $10^{-18.62\pm0.14}$, respectively, with the value of the postburst being smaller than the main burst. Figure 10 also shows GRB 130427A that $\Re$ of the main burst increases first and then decreases over time, and the postbursts also extend the main burst. The mean values of the main bursts and postbursts $\Re$ are $10^{-18.56\pm0.38}$ and $10^{-18.57\pm0.08}$, respectively, and the two values are almost the same.

5.2. Parameter Γ

The Lorentz factor for the gliding phase($r_{\rm ph} > r_s$) can be given by

$$\Gamma \propto (F/\Re)^{1/4} Y^{1/4}, \tag{6}$$

where Y relates to the radiative efficiency of the burst, which is given by

$$Y = \frac{L_0}{L_{\rm obs,\gamma}}, \tag{7}$$

where L_0 is the total kinetic luminosity and $L_{\rm obs,\gamma}$ is the observed gamma-ray luminosity.

The evolution of Γ over time for GRB 160509A and GRB 130427A is given in Figure 11. From the figure we can see that the Γ of the main burst of GRB 160509A increases first and then decreases over time. The mean values for the main bursts and postbursts are $10^{2.36\pm0.09} Y^{1/4}$ and $10^{2.07\pm0.12} Y^{1/4}$. The Γ value for the main burst is greater than that of the postburst, in line with the predictions of the fireball model. The Γ of the main burst of GRB 130427A in Figure 11 has a clear trend from increasing to decreasing with time, and the Γ of the postburst $10^{2.19\pm0.04} Y^{1/4}$ is much smaller than the main burst ($10^{2.53\pm0.16} Y^{1/4}$).

5.3. Parameters r_0, r_s, and r_{ph}

The nozzle radius r_0 indicates the radius at which the jet starts to accelerate and, after obtaining $\Re$. The formula for r_0 given for $r_{\rm ph} > r_s$ is as follows (Pe'Er et al. 2007):

$$r_0 \propto (F_{\rm BB}/FY)^{3/2} \Re. \tag{8}$$

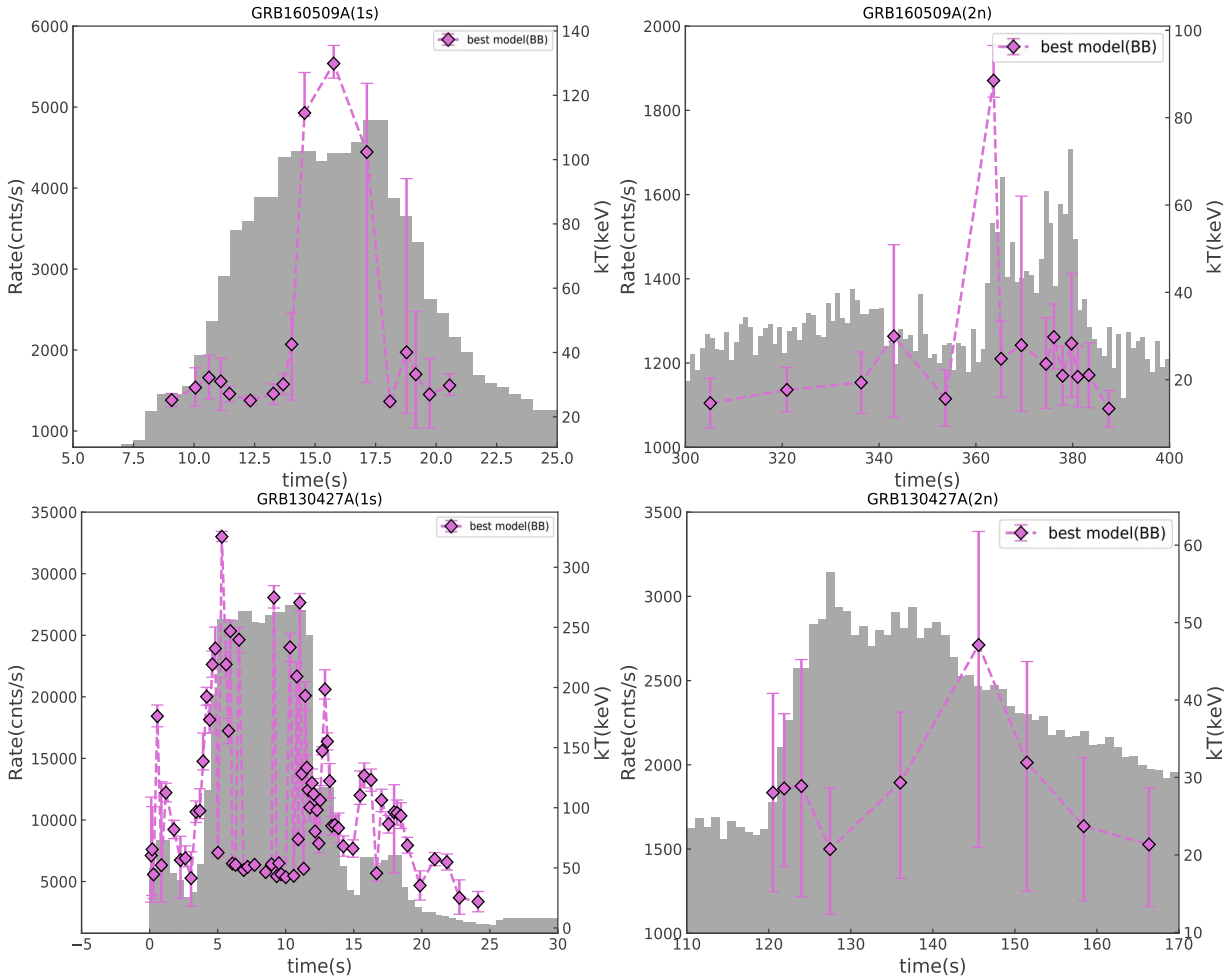

Figure 5. Evolution of the spectral parameter kT over time fitted with the best model. All symbols are the same as in Figure 3.

The saturation radius r_s represents the radius at which the Lorentz factor reaches its maximum, and with r_0 we can obtain an estimate of the saturation radius r_s, which is given by the following equation:

$$r_s = \Gamma r_0. \tag{9}$$

Considering relativistic holonomic motion, for photons propagating at a distance ds, the optical depth τ is given by

$$\tau = \int_{r_{\rm ph}}^{\infty} \frac{n\sigma_T}{2\Gamma^2} dr, \tag{10}$$

where σ_T is the Thompson cross section and n is the electron number density. $ds = (1 - \beta\cos\theta)dr/\cos\theta$, where $\theta = 0$. Assuming a constant Lorentz factor, the radius of the photosphere can be calculated by the following equation ($\tau = 1$):

$$r_{\rm ph} = \frac{L_0\sigma_T}{8\pi m_p c^3 \Gamma_{\rm ph}^3}, \tag{11}$$

where L_0 is the total kinetic luminosity, given by $L_0 = 4\pi d_L^2 YF_{\rm tot}$, where d_L is the luminosity distance and F_{tot} is the observed γ-ray flux.

The evolution of r_0, r_s, and $r_{\rm ph}$ over time is illustrated in Figure 12. For GRB 160509A the mean values of the radii of the main burst features (r_0, r_s, $r_{\rm ph}$) are $10^{7.36\pm0.67}Y^{3/2}$, $10^{9.72\pm0.68}Y^{3/2}$, and $10^{11.78\pm0.24}Y^{5/4}$ cm. The mean characteristic radii of postbursts are all smaller than that of the main bursts, and their values are $10^{7.05\pm0.59}Y^{3/2}$, $10^{9.12\pm0.60}Y^{3/2}$, and $10^{11.19\pm0.16}Y^{5/4}$ cm, respectively. For the GRB 130427A, the characteristic radii of the main bursts are $10^{7.84\pm0.62}Y^{3/2}$, $10^{10.37\pm0.68}Y^{3/2}$ and $10^{11.71\pm0.39}Y^{5/4}$ cm, respectively. The characteristic radii of the postbursts are $10^{6.90\pm0.66}Y^{3/2}$, $10^{9.09\pm0.65}Y^{3/2}$ and $10^{11.35\pm0.09}Y^{5/4}$ cm, respectively, and the values of the postbursts are smaller than those of the main bursts. From the figure, we can see that the main bursts have the trend of transition to the postbursts.

6. Discussion

GRB 160509A and GRB 130427A with such clearly separated events have distinct time-resolved spectral properties, providing clues to the central engine of GRBs. Through time-resolved spectra analysis, Ryde et al. (2010) found that the GRB 090902B has a fireball feature and was characterized by a multicolor blackbody or Planck function. As time goes by, the spectrum broadens and the photosphere radius increases, which may be expressed as a gradual change in jet composition. Zhang et al. (2016) showed that the jet dominated by Poynting flux in GRB 130606B is only characterized by the Band function. In addition, Axelsson et al. (2012) also found in GRB 110721A a mixed jet with synchrotron radiation-dominated thermal components and subdominated jet components. Ghirlanda et al. (2003) showed that bright GRBs such as GRB 911118, GRB 910807, and GRB 910927 exhibit thermal

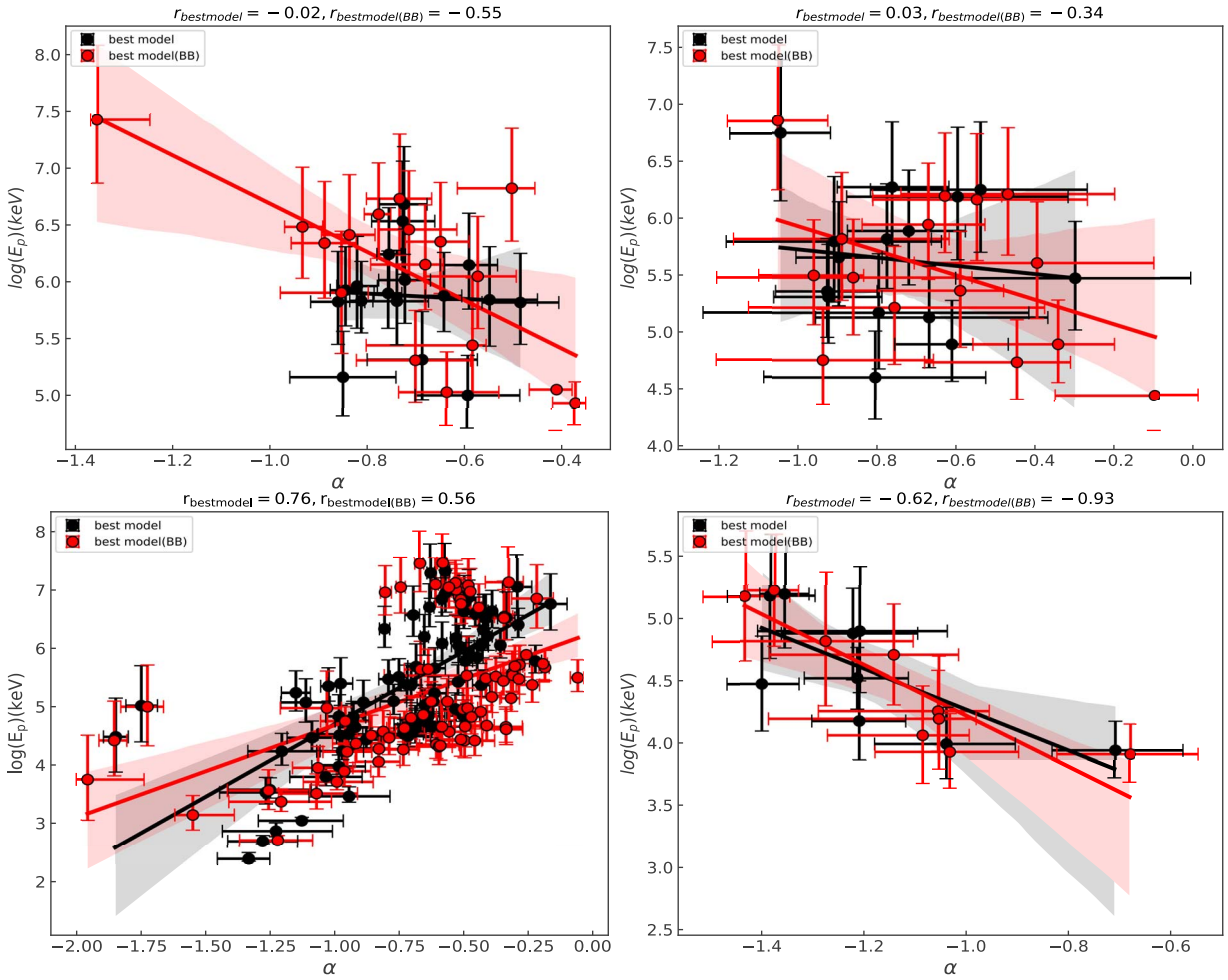

Figure 6. Correlations between α and E_p fitted with the best model for the two bursts. Black and red data points represent best model and best model+BB, respectively. Top left and right panels are the main bursts and postbursts in GRB 160509A, while bottom left and right panels are the main bursts and postbursts in GRB 130427A.

spectra at the onset or near their peaks, while nonthermal spectra exist throughout the burst event. Zhang et al. (2018) and Li (2019) found that GRB 160625B exhibits a strong change in jet composition, indicating a transition from fireball to Poynting flux dominated.

In the GRB 160509A and GRB 130427A studied in this paper, the main burst has a strong thermal component, and the postburst is nonthermal. After adding the BB component, the time slices of α exceeds the synchrotron radiation dead line for the main burst increases and Li (2019) came to the same conclusion, indicating that the thermal fireball dominates, and the postburst is little or nonexistent, suggesting a magnetic domination. Therefore, it can also be speculated that these two GRBs with both main bursts and postbursts are transitions from fireballs to Poynting flux dominance.

The apparent change in the composition of the jet reveals the nature of the GRB central engine. From the Wang & Mészáros (2007) analysis of the jets of GRBs precursors and main bursts we speculate that the superaccretion of the central engine of GRBs with main bursts and postbursts forms a matter-dominated fireball through neutrino–antineutrino annihilations during the first burst. The jets are intermittent, and after the main burst (rapid accretion phase), the central engine enters a quiescent phase. Proga & Zhang (2006) speculated that energy release can be achieved by repeated accretion of the accumulated flux around the central engine, which starts up again after the main burst and is strongly magnetized, thus manifesting itself as synchrotron radiation that powers the second burst event (postburst) like the remarkable late X-ray flares shown by the GRBs.

The discovery of precursors is important for the understanding of the origin and properties of GRBs, and Lazzati & Begelman (2005), in agreement with Koshut et al. (1995), found no correlation between precursor and main burst properties, and that the precursor spectrum is a nonthermal power law, making it difficult to explain the precursor model. For the present paper the postburst is also a nonthermal spectrum and it is not possible to tell from our analysis whether it has the same origin as main burst. Hu et al. (2014) found comparable spectral indices by analyzing the spectra of precursors and main bursts, suggesting that these different radiation events may have the same physical origin and therefore be a duplicated activation of the central engine of the GRB. For the GRBs studied in this paper, the spectral indices are not correlated, and it is speculated that the main bursts and postbursts may have different origins. Coppin et al. (2020) analyzed 217 GRBs with precursors and found that the quiescent time profile, given by the time between the precursor and the main burst, is well described by a double Gaussian distribution, indicating that the observed precursors have two

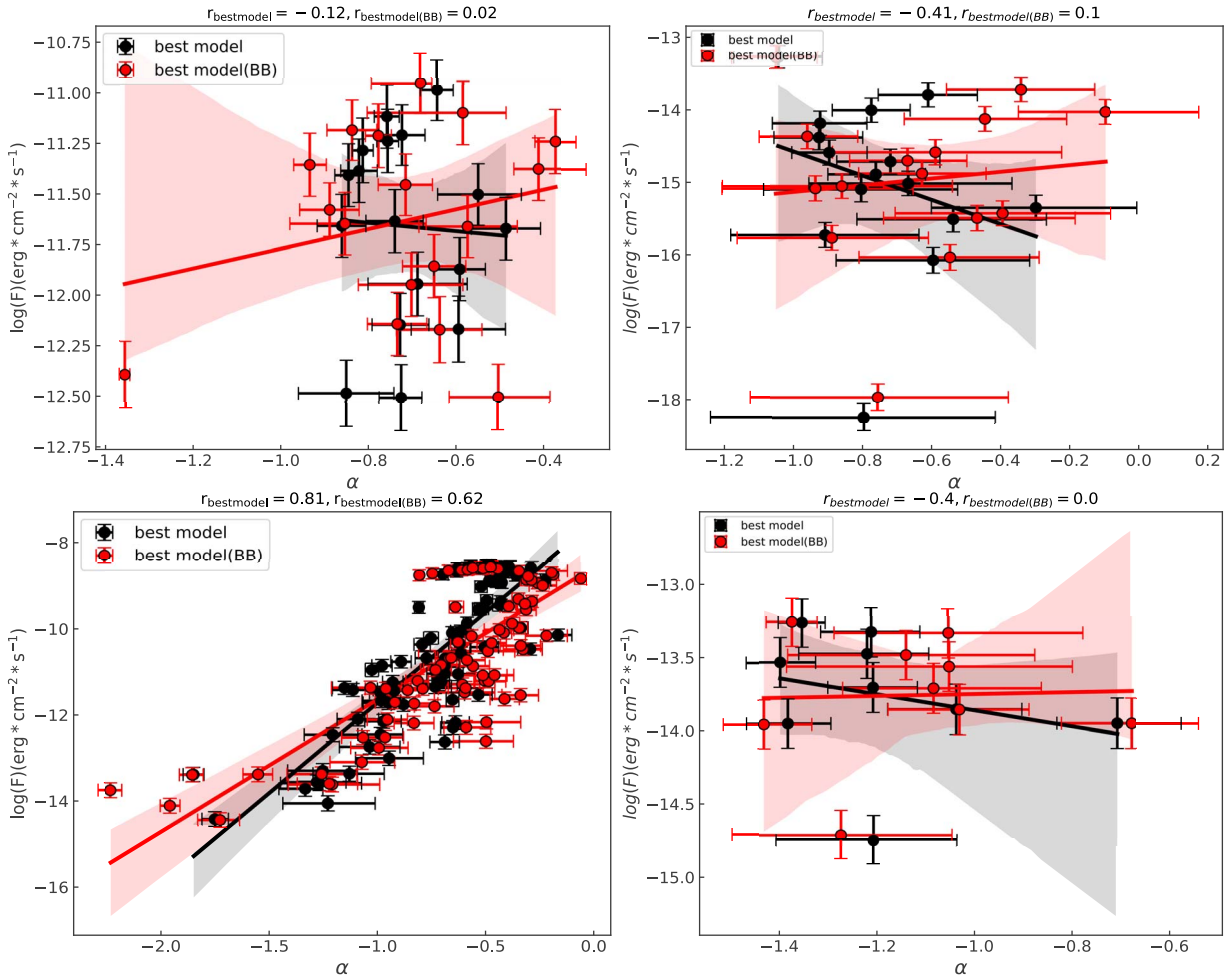

Figure 7. Correlations between α and F fitted with the best model for the two bursts. All symbols are the same as in Figure 6.

distinct physical progenitors. The GRBs studied in this paper are numerically small and therefore do not have statistical findings. Li et al. (2021) studied short burst events with simultaneous precursors, main bursts, and extended radiation, and they found a correlation between the peak fluxes of precursors, main bursts, and extended radiation, thus supporting the idea that the three events came from similar central engines. In this paper the higher the peak flux of the main burst, the higher the peak flux of the postburst, so it seems to show a correlation between the peak flux of the main burst and the postburst, and so may indicate that the main bursts and postbursts are of the same origin.

Ryde et al. (2010) demonstrated that thermal radiation can be used to study the properties of photospheres, thereby studying the physical parameters of GRB fireballs. Pe'er et al. (2015) derived the range of the bulk Lorentz factor Γ and the initial radius r_0 from 47 GRBs in the framework of the fireball model, and they obtain the following ranges of Γ and r_0: $10^2 \leqslant \Gamma \leqslant 10^3$, $10^{6.5} \leqslant r_0 \leqslant 10^{9.5}$. The conclusions obtained in this paper are the same. The absence of a thermal component in the postbursts is consistent with the parameter range and further analysis is needed. And the evolution of the parameters shows that there is a trend toward a transition from the main burst to the postburst. But there is no clear evidence that the main burst and the postburst are of the same origin.

GRB 160509A and GRB 130427A are two of the GRBs that have postbursts. They show different quiescent times and have different durations of outburst events. Zhang et al. (2018) showed quiescent times of 180 s for the GRB 160625B precursor and main burst and 339 s between the main burst and extended radiation. The quiescent times for precursors earlier than the main burst in long GRBs detected by the BATSE is observed to range from the typical tens of seconds to 200 s and usually has a nonthermal power-law spectrum. Further studies are needed to determine the length of the quiescent times or the relationship between quiescent time and radiation time for main bursts and postbursts.

The parameters derived from this paper have a hard-to-soft variation with time and a tracking behavior, which is the same as the conclusion reached by Li (2019). And the negative correlation between the main burst parameters $\alpha - E_p$ of GRB 160509A is also in line with Li (2019), who concluded that both positive and negative correlations of $\alpha - E_p$ are possible.

Using the spectral data observed by Fermi GBM, our spectral analysis of GRB 130427A and GRB 160509A shows that the thermal component mainly exists in the main burst, and the postburst is dominated by the nonthermal component. These characteristics indicate that the radiation of the main burst is contributed by the photosphere radiation and the internal shock of the relativistic jet (Giannios 2008; Lazzati & Begelman 2010; Beloborodov 2010). The radiation of the postburst is caused by the internal and external shock waves of the relativistic jet (Sari et al. 1998; Kumar & Panaitescu 2000; Kobayashi et al. 2007; Becerra et al. 2019). Similar to GRB

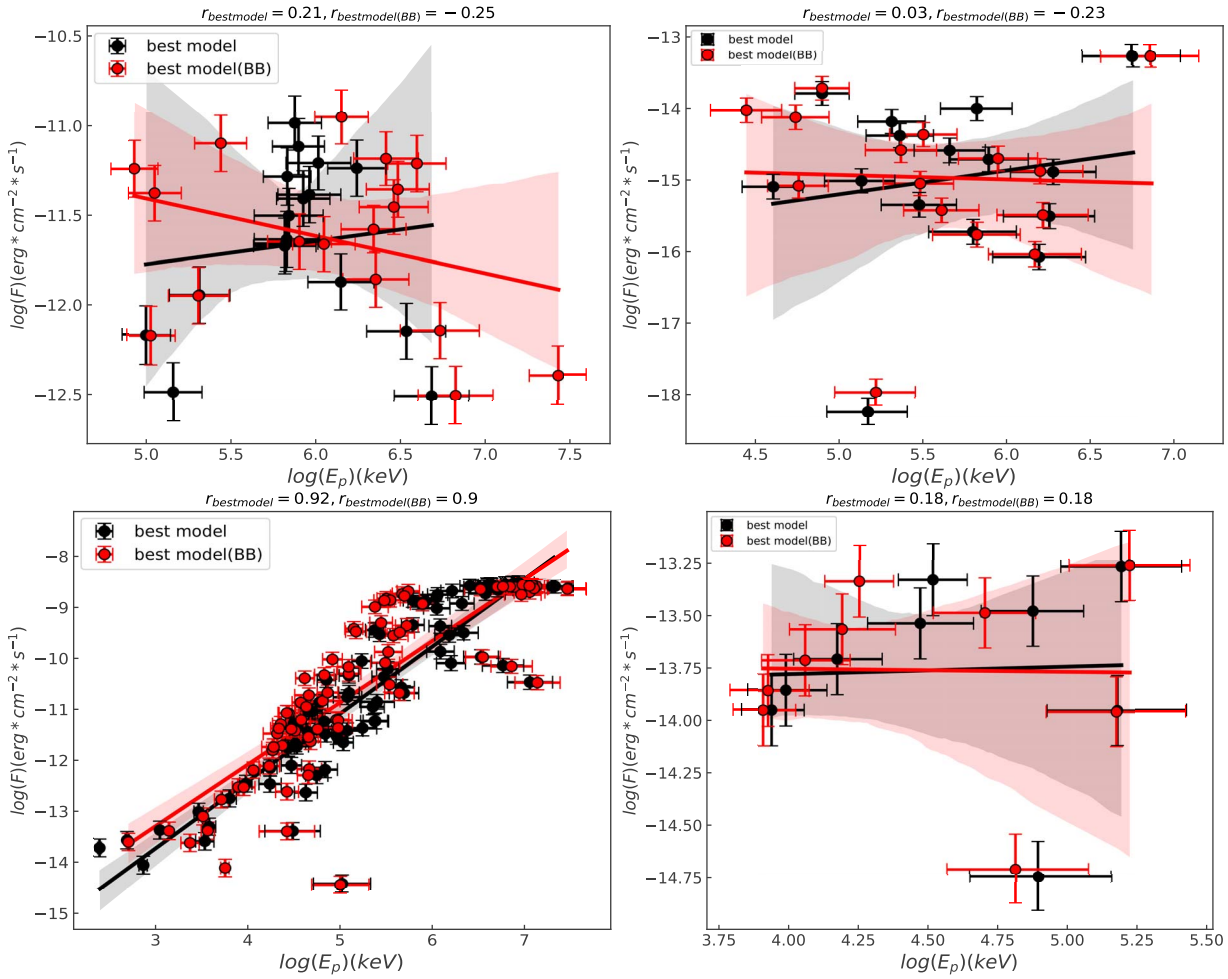

Figure 8. Correlations between E_p and F fitted with the best model for the two bursts. All symbols are the same as in Figure 6.

130427A and GRB 160509A, GRB 160625B is also a GRB with main burst and postburst. Lu et al. (2017) used GBM and LAT data to analyze the main burst (episode II) and postburst (episode III) of this burst. Their analysis results are similar to ours, that is, the main burst has thermal components and the postburst does not. The physical processes of these two stages are different. That is, episode II may be from photosphere emission and internal shock of the relativistic jet, and episode III is contributed by internal and external shocks of the relativistic jet. Moreover, Lu et al. (2017) found that the spectra observed by LAT was different from that observed by GBM. They speculated that this LAT component is a high-energy afterglow, and that the steady increase in LAT flux may be the beginning of the high-energy afterglow, which was soon confirmed by Fraija et al. (2017). They studied the observations during GRB 160625B episode II (early afterglow) and III (late afterglow) using multiwavelength (LAT, XRT, and UVOT) observation data. Fraija et al. (2017) used an early afterglow external shock model in the stellar wind medium and the interstellar medium (ISM) to describe multiwavelength observations during GRB 160625B events II (early afterglow) and III (late afterglow). They pointed out that the multiwavelength observations of event II are consistent with the evolution of the afterglow in the stellar wind medium; synchrotron radiation from the reverse shock and synchrotron self-Compton radiation are required to explain the GeV gamma-ray and optical observations in the early afterglow. Whereas the observations at event III are consistent with the evolution of the afterglow in the ISM, and the optical and X-ray flux of the late afterglow coincides with the synchrotron radiation from the adiabatic forward shock.

Similar to GRB 160625B, GRB 130427A and GRB 160509A also have a bright peak (GeV flare) after the end of the main burst. The observed GeV flare should be an early afterglow, which is different from the origin of the postburst (late afterglow) we analyzed. Fraija et al. (2020) studied the LAT observation results of GRB 160509A and found that the light curve of LAT showed the inflection of GeV flare and persistent radiation, and two very high-energy photons (VHE) with energy of 51.9 and 41.5 GeV were observed at 76.5 and 242 s after the outbreak. They showed that GeV flare is consistent with the Synchrotron self-Compton (SSC) reverse shock model, and that VHE (VHE $\geq$ 1 GeV) photons are generated by SSC radiation from the forward shock. The same SSC model also well explains the GeV flare of GRB 130427A (Fraija et al. 2022). The standard synchrotron radiation forward shock model successfully explains the GRB afterglow observation. However, the photon energy is higher than 10 GeV, which can hardly be described in the synchrotron radiation model. Fraija et al. (2022) proposed the closure relations of the SSC afterglow model under adiabatic and radiative conditions and when the central engine injects continuous energy into the shock wave to study the spectral and time exponential evolution of these bursts. They found that

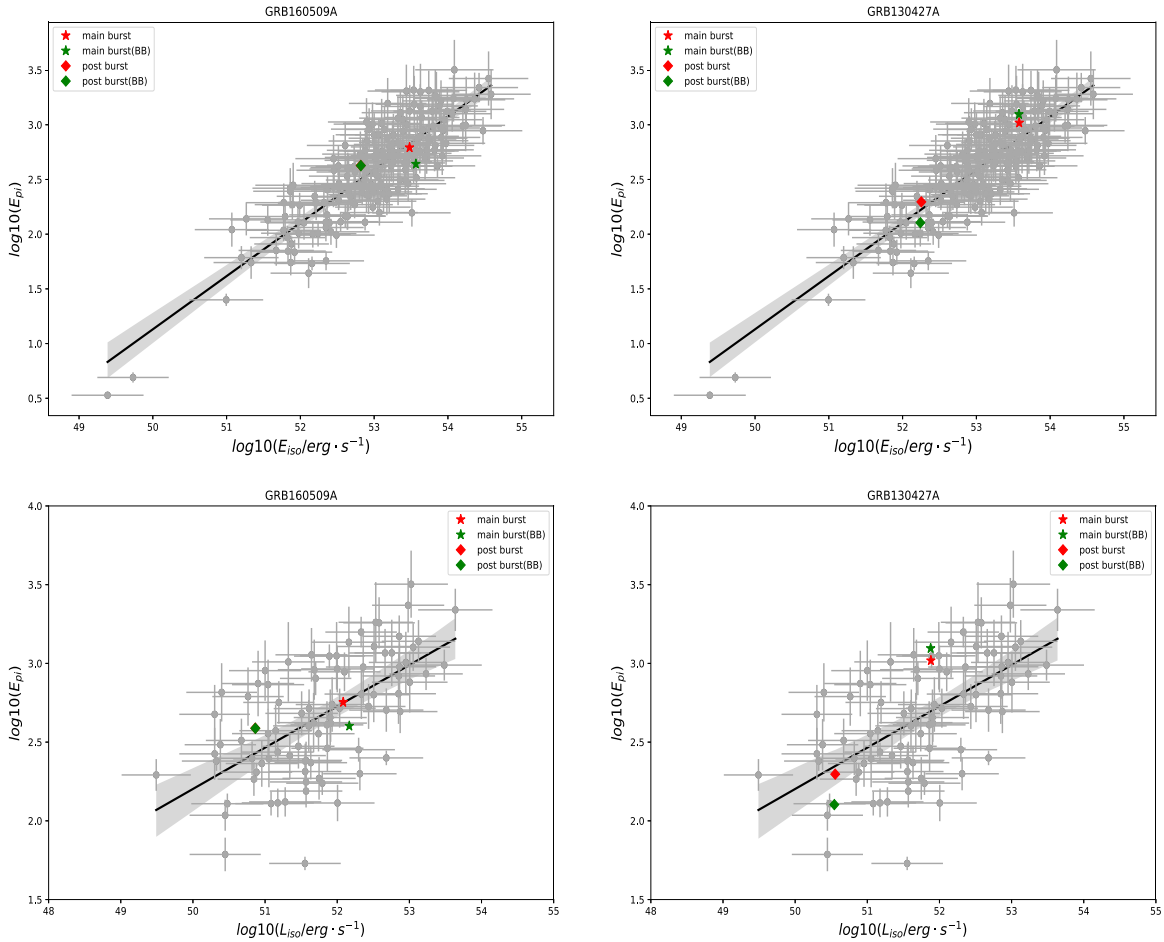

Figure 9. Amati and Yonetoku relations for GRB 160509A (left panel) and GRB 130427A (right panel), where the red pentagons represent the best model for the main burst, red diamonds represent the postburst, the green pentagons represent the main burst with BB, and the green diamonds represent the postbursts with BB.

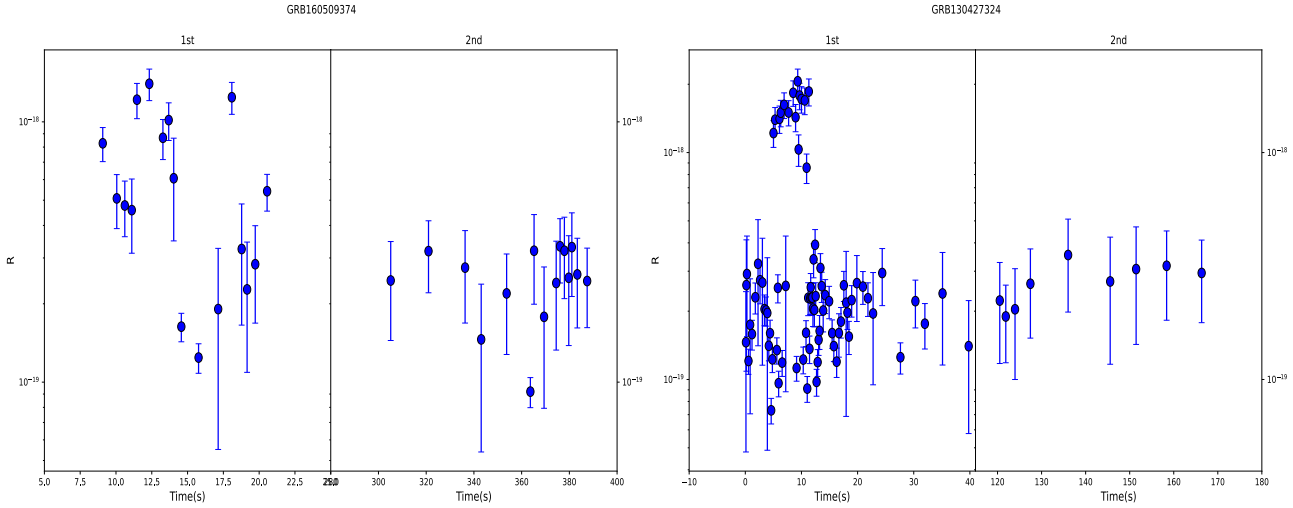

Figure 10. Evolution of $\mathfrak{R}$

the closure relations of the SSC model satisfied most of the unexplained bursts in the synchrotron model.

In this paper, we only analyze the spectral data detected by GBM. Therefore, our physical interpretation is different from that of Fraija et al. (2020) and Fraija et al. (2022). The above research shows that the radiation of the main burst and the postburst may be dominated by different physical processes; that is, the nonthermal radiation of the main burst and the postburst, in addition to the synchrotron radiation, also contributes to the SSC radiation in the early afterglow. In order to better understand the physical origin of the main burst and the postburst, we should combine the GBM and LAT and

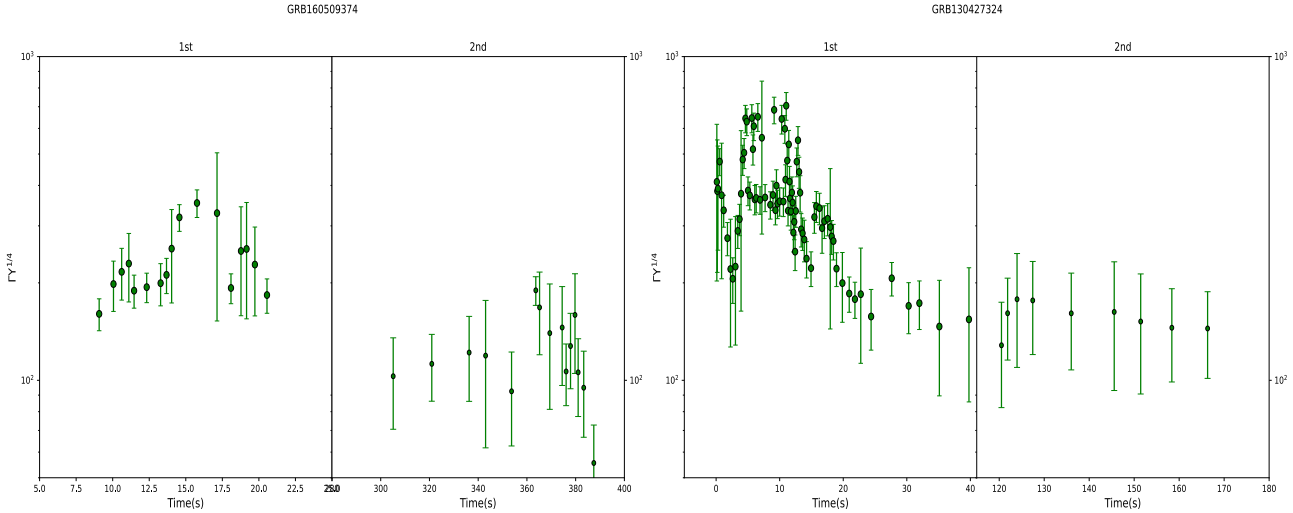

Figure 11. Evolution of Γ

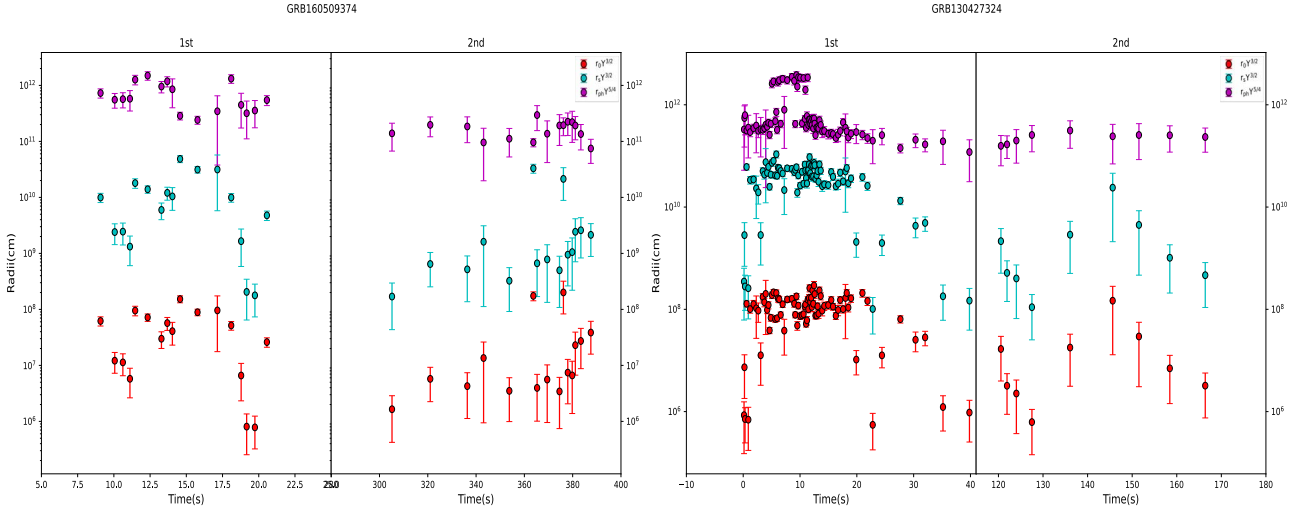

Figure 12. Evolution of r_0, r_s, and $r_{\rm ph}$

the afterglow data for analysis. Therefore, in the future work, we would combine GBM and LAT and afterglow data to analyze the spectra of the main burst and postburst, and further understand the radiation mechanism of the main burst and the postburst.

7. Conclusion

In this paper, we perform a Bayesian time-resolved spectral analysis of GRB 160509A and GRB 130427A with main bursts and postbursts, by means of the Band and CPL models. The thermal component analysis reveals that the main bursts of both GRBs contain a significant thermal component, while the postbursts have a much weaker thermal component. Our comparative analysis of the spectral and photospheric properties of the main bursts and postbursts of these two bursts yield the following interesting conclusions:

1. The main bursts of GRB 130427A and GRB 160509A have a significant thermal component at 90% and 53%, respectively, while in both postbursts only one bin has a thermal component. In addition, the main bursts of both bursts had bins exceeding the so-called synchronous dead line in 51.85% (42/81) and 29.41% (5/17) of the bursts, respectively. In the postbursts, only GRB 160509A had four bins exceed the dead line (26.67%), while none of GRB 130427A had bins over the dead line. Indicating that these two GRBs its energy spectral properties reveal a transition from fireball-dominated to Poynting-flux-dominated jet composition.
2. After adding BB components, for the case of GRB 160509A, for the main burst the number of $\alpha > -2/3$ increased by 2, and the corresponding number of postbursts increased by 4; for GRB 130427A, the number of $\alpha > -2/3$ increases by 12, and none of the postbursts exceed the synchrotron radiation dead line. It once more shows that the thermal component is gradually decreasing and the jet composition has changed from the main bursts to the postbursts.
3. We use the photospheric radiation parameters to constrain the main bursts and postbursts of GRB 160509A and GRB 130427A and find that the photospheric radiation parameters ($\mathfrak{R}$, Γ, r_0, r_s and $r_{\rm ph}$) of the postbursts are smaller compared to the main bursts. And there is a trend of transition from the main burst to the postburst.
4. Our analysis of the evolutionary behavior of the spectral parameters (α, E_p) reveals that there is no significant consistent evolutionary behavior over time for α in both

the main bursts and postbursts for the GRB 160509A and GRB 130427A. For GRB 160509A, E_p in the main burst has similar hard-to-soft pattern in main burst and postburst. While for the GRB 130427A, E_p first evolves in a hard-to-soft at the beginning, followed by an evolutionary behavior of tracking flux, and there is a hard-to-soft trend in the postburst. The main burst and the postburst of kT have similar tracking evolutionary behavior for both the two bursts.

5. By analyzing the correlations between the spectral parameters, we find that there is no correlation between $\alpha - E_p$, $\alpha - F$, and $E_p - F$ in both the main bursts and postbursts of GRB 160509A; in GRB 130427A, there is a strong correlation between $\alpha - E_p$ in the main burst; however, the postbursts show a strong negative correlation. Similarly, $\alpha - F$ and $E_p - F$ are positively correlated in the main burst, but not in the postburst. The above results suggest that the main bursts and postbursts of GRB 160509A may be of the same origin, while the main bursts and postbursts of GRB 130427A may be of different origin. The fact that the time-integrated spectra of both the main bursts and postbursts of GRB 160509A and GRB 130427A are consistent with the Amati relation and Yonetoku relation suggests that the main bursts and postbursts of the two GRBs may come from the same origin. Therefore, we cannot determine whether the main bursts and postbursts come from the same origin based on the analysis of the spectral properties of the two bursts.

Therefore, we need much larger sample to reveal the nature of the main bursts and postbursts, which deserves the further investigation.

We thank the anonymous referee for valuable suggestions that helped to improve the paper. We acknowledge the use of the public data from the Fermi data archives. This work is supported by the National Natural Science Foundation of China (grant 12163007, 11763009), the Key Laboratory of Colleges and Universities in Yunnan Province for High-energy Astrophysics, National Astronomical Observatories Yunnan Normal University Astronomical Education Base, Graduate Research and Innovation Fund of Yunnan Normal University.

ORCID iDs

Zhao-Yang Peng https://orcid.org/0000-0003-3846-0988

References

Axelsson, M., Baldini, L., Barbiellini, G., et al. 2012, ApJL, 757, L31
Band, D., Matteson, J., Ford, L., et al. 1993, ApJ, 413, 281
Becerra, R. L., Dichiara, S., Watson, A. M., et al. 2019, ApJ, 881, 12
Bégué, D., & Pe'er, A. 2015, ApJ, 802, 134
Beloborodov, A. M. 2010, MNRAS, 407, 1033
Beniamini, P., & Piran, T. 2013, ApJ, 769, 69
Beniamini, P., & Piran, T. 2014, MNRAS, 445, 3892
Burgess, J. M. 2014, MNRAS, 445, 2589
Burgess, J. M., & Ryde, F. 2015, MNRAS, 447, 3087
Charisi, M., Márka, S., & Bartos, I. 2015, MNRAS, 448, 2624
Coppin, P., de Vries, K. D., & van Eijndhoven, N. 2020, PhRvD, 102, 103014
Daigne, F., Bošnjak, Ž., & Dubus, G. 2011, A&A, 526, A110
Daigne, F., & Mochkovitch, R. 1998, MNRAS, 296, 275
Di Matteo, T., Perna, R., & Narayan, R. 2002, ApJ, 579, 706
Ellison, D. C., Baring, M. G., & Jones, F. C. 1995, ApJ, 453, 873
Fraija, N., Dainotti, M. G., Ugale, S., et al. 2022, ApJ, 905, 188
Fraija, N., Laskar, T., Dichiara, S., et al. 2020, ApJ, 905, 112
Fraija, N., Veres, P., Zhang, B. B., et al. 2017, ApJ, 848, 15
Gao, H., & Zhang, B. 2015, ApJ, 801, 103
Ghirlanda, G., Celotti, A., & Ghisellini, G. 2003, A&A, 406, 879
Giannios, D. 2008, A&A, 488, L55
Goodman, J. 1986, ApJL, 308, L47
Granot, J., Komissarov, S. S., & Spitkovsky, A. 2011, MNRAS, 411, 1323
Gu, W.-M., Liu, T., & Lu, J.-F. 2006, ApJL, 643, L87
Hu, Y.-D., Liang, E.-W., Xi, S.-Q., et al. 2014, ApJ, 789, 145
Katz, J. I. 1994, ApJ, 422, 248
Kobayashi, S., Zhang, B., Mészáros, P., & Burrows, D. 2007, ApJ, 655, 391
Koshut, T. M., Kouveliotou, C., Paciesas, W. S., et al. 1995, ApJ, 452, 145
Kumar, P., & McMahon, E. 2008, MNRAS, 384, 33
Kumar, P., & Panaitescu, A. 2000, ApJL, 541, L51
Kumar, P., & Zhang, B. 2015, PhR, 561, 1
Lazzati, D., & Begelman, M. C. 2005, ApJ, 629, 903
Lazzati, D., & Begelman, M. C. 2010, ApJ, 725, 1137
Li, L. 2019, ApJS, 242, 16
Li, X. J., Zhang, Z. B., Zhang, X. L., & Zhen, H. Y. 2021, ApJS, 252, 16
Liu, T., Gu, W.-M., Xue, L., & Lu, J.-F. 2007, ApJ, 661, 1025
Liu, T., Gu, W.-M., & Zhang, B. 2017, NewAR, 79, 1
Lloyd, N. M., & Petrosian, V. 2000, AAS HEAD Meeting, 5, 34.03
Lu, H.-J., Lu, J., Zhong, S.-Q., et al. 2017, ApJ, 849, 71
Paczynski, B., & Xu, G. 1994, ApJ, 427, 708
Pe'er, A., Barlow, H., O'Mahony, S., et al. 2015, ApJ, 813, 127
Pe'Er, A., Mészáros, P., & Rees, M. J. 2007, RSPTA, 365, 1171
Popham, R., Woosley, S. E., & Fryer, C. 1999, ApJ, 518, 356
Proga, D., & Zhang, B. 2006, MNRAS, 370, L61
Rees, M. J., Meszaros, P., & Begelman, M. C. 1994, in AIP Conf. Ser. 307, Gamma-Ray Bursts, ed. G. J. Fishman (Melville, NY: AIP), 605
Ruffini, R., Salmonson, J. D., Wilson, J. R., & Xue, S.-S. 1999, A&AS, 138, 511
Ruffini, R., Salmonson, J. D., Wilson, J. R., & Xue, S. S. 2000, A&A, 359, 855
Ryde, F., Axelsson, M., Zhang, B. B., et al. 2010, ApJL, 709, L172
Ryde, F., & Pe'er, A. 2009, ApJ, 702, 1211
Sari, R., Narayan, R., & Piran, T. 1996, ApJ, 473, 204
Sari, R., Piran, T., & Narayan, R. 1998, ApJL, 497, L17
Scargle, J. D., Norris, J. P., Jackson, B., & Chiang, J. 2013, ApJ, 764, 167
Spitkovsky, A. 2008, ApJL, 682, L5
Tavani, M. 1996, ApJ, 466, 768
Troja, E., Rosswog, S., & Gehrels, N. 2010, ApJ, 723, 1711
Vianello, G. 2018, ApJS, 236, 17
Vianello, G., Lauer, R. J., Younk, P., et al. 2015, arXiv:1507.08343
Wang, X.-Y., & Mészáros, P. 2007, ApJ, 670, 1247
Xue, L., Liu, T., Gu, W.-M., & Lu, J.-F. 2013, ApJS, 207, 23
Yu, H.-F., Hui, C. Y., Kong, A. K. H., & Takata, J. 2018, ApJ, 857, 120
Zhang, B. 2011, NuPhS, 221, 324
Zhang, B., & Yan, H. 2011, ApJ, 726, 90
Zhang, B.-B., Uhm, Z. L., Connaughton, V., Briggs, M. S., & Zhang, B. 2016, ApJ, 816, 72
Zhang, B.-B., Zhang, B., Castro-Tirado, A. J., et al. 2018, NatAs, 2, 69
Zhong, S.-Q., Dai, Z.-G., Cheng, J.-G., Lan, L., & Zhang, H.-M. 2019, ApJ, 884, 25